CRYSTAL GROWTH & DESIGN

Article

1D and 2D silver-based coordination polymers with thiomorpholine-4-carbonitrile and aromatic polyoxoacids as co-ligands: structure, photocatalysis, photoluminescence and TD-DFT study

Predrag Risti#, Tamara R. Todorovic, Vladimir Blagojevi#, Olivera R. Klisuric, Ivana Marjanovi#, Berta Barta Holló, Predrag Vulic, Mihaela Gulea, Morgan Donnard, Miguel Monge, María Rodríguez-Castillo, Jose M. Lopez-De-Luzuriaga, and Nenad R. Filipovic

Cryst. Growth Des., **Just Accepted Manuscript** • DOI: 10.1021/acs.cgd.0c00287 • Publication Date (Web): 20 May 2020

Just Accepted

is published by the American Chemical Society. 1155 Sixteenth Street N.W., Washington, DC 20036

1D and 2D silver-based coordination polymers with thiomorpholine-4-carbonitrile and aromatic polyoxoacids as co-ligands: structure, photocatalysis, photoluminescence and TD-DFT study

Predrag Ristić[a], Tamara R. Todorović[a,*], Vladimir Blagojević[b], Olivera R. Klisurić[c], Ivana Marjanović[c], Berta Barta Holló[c], Predrag Vulić[d], Mihaela Gulea[e], Morgan Donnard[f], Miguel Monge[g], María Rodríguez-Castillo[g], José M. López-de-Luzuriaga[g], Nenad R. Filipović[h]

[a] *University of Belgrade - Faculty of Chemistry, Studentski trg 12-16, 11000 Belgrade, Serbia*

[b]*Institute of Technical Sciences of the Serbian Academy of Sciences and Arts, Knez Mihailova 35/IV, 11000 Belgrade, Serbia*

[c] *University of Novi Sad, Faculty of Sciences, Trg Dositeja Obradovića 4, 21000 Novi Sad, Serbia*

[d]*Faculty of Mining and Geology, University of Belgrade, Đušina 5, 11000 Belgrade, Serbia*

[e]*Université de Strasbourg, CNRS, LIT – UMR 7200, Faculty of Pharmacy, 67000 Strasbourg, France*

[f]*Université de Strasbourg, Université de Haute-Alsace, CNRS, LIMA – UMR 7042, ECPM, 67000 Strasbourg, France*

[g] *Departamento de Química, Universidad de La Rioja, Centro de Investigación en Síntesis Química (CISQ), Complejo Científico-Tecnológico, 26004-Logroño, Spain*

[h]*University of Belgrade - Faculty of Agriculture, Nemanjina 6, 11000 Belgrade, Serbia*

*Corresponding author: Tamara R. Todorović, PhD, Associate Professor, University of Belgrade - Faculty of Chemistry, Studentski trg 12-16, 11000 Belgrade, Serbia; E-mail: tamarat@chem.bg.ac.rs

Abstract

Four silver-based coordination polymers $\{[Ag(L)_2](BF_4)\}_\infty$ (**1**), $\{[Ag(H_2BTC)(L)]\times(H_3BTC)\}_\infty$ (**2**), $\{[Ag_2(H_2BTEC)(L)_2] \times 3.33H_2O\}_\infty$ (**3**) and $[Ag(H_25SSA)(L)]_\infty$ (**4**) were synthesized using thiomorpholine-4-carbonitrile (L) as the primary ligand and three aromatic polyoxoacids as co-ligands: trimesic (H_3BTC), pyromellitic (H_4BTEC) and 5-sulfosalicylic acid (H_35SSA). Compounds **1** and **3** are two-dimensional, while **2** and **4** are one-dimensional. L acts as a *bis*-monodentate ligand, while Ag(I) ion is three-coordinated in **2**, and four-coordinated in all the other compounds. Tetrahedral coordination of Ag(I) in **3** leads to an almost complete absence of intermolecular interactions with the metal center. All compounds show reasonable photocatalytic activity for photocatalytic degradation of mordant blue 9 dye, with reaction rates in 0.036–0.056 min^{-1} range. Changes in the reaction rates can be correlated with the type and coordination of the co-ligand. Complex **3** exhibits photoluminescence at 77 K, while **4** exhibits photoluminescence at both room temperature and 77 K. Luminescence lifetimes indicate electronic transitions of singlet parentage, where transitions are allowed. TD-DFT study determined the contributions of individual singlet-singlet electronic excitations to the fluorescence, indicating that metal- intra ligand transitions is responsible for luminescence in both complexes.

Keywords: Silver complexes; Coordination polymers; Intermolecular interactions; Photoluminescence; Photocatalysis; TD-DFT.

1. INTRODUCTION

The investigation of coordination polymers (CPs) is a rapidly growing field of material science. 1D–3D CPs have been studied because of the wide range of potential applications, predominantly in catalysis, gas storage and separation, optoelectronics and sensors, molecular electronics, nanomaterial synthesis, illumination and photodetection.[1–15] Silver is among the top ten metals used for the preparation of 2D CPs,[16,17] while 8 % of all CPs (1D–3D) deposited in CSD MOFs subset[18] are Ag-CPs. The ability to adopt coordination numbers from 2 to 6, thus offering various coordination geometries, makes silver a viable metal of choice for the synthesis of CPs.[19] In addition, coordination numbers higher than six have been observed in some of Ag-CPs.[20,21] Structural diversity of Ag-CPs is not only influenced by supramolecular Ag···ligand, Ag···π, C–H···π, π-π stacking and anion interactions, as well as H-bonds,[22,23] but also by

argentophilic (Ag···Ag) and Ag···C interactions.[24,25] Finally, the structures of Ag-CPs are heavily influenced by the nature of the anion of the starting silver salt.[26–30] In the case of 1D Ag-CPs, linear, zigzag, helical, ladder and 1D coordination tubes have been identified.[22] In 2013, the first ribbon topology was observed for one 1D Ag-CP.[31] More recently, the structure with metal cluster topology was discovered,[32] making rotaxane topology the only unrealized topology type of 1D Ag-CPs up to now. On the other hand, representative topologies of 2D Ag-CPs include **sql** and **hcb**.[18]

Ag-CPs may undergo structural transformation induced by light,[33] heating,[34,35] solvation,[36–40] desolvation,[35] guest molecule[40,41] and anion exchange[26,36,42,43] stimuli. They can be used as precursors for the preparation of Ag nanoparticles by heating[25,44] or ultrasonic irradiation.[45] Some of the investigated Ag-CPs form metallogels[28,46–52] showing interesting properties, such as the ability to sense hazardous gases.[49] Metallogels can also act as precursors for Ag-based nanoparticles which can be obtained in situ,[49] spontaneously[46] or upon exposure to light.[50] These nanoparticles exhibit luminescence properties,[51] as well as the ability to be reversibly assembled or disassembled by various stimuli.[52] Finally, Ag-CPs metallogels can display thixotropic behavior,[47] stimuli-responsive to some anions as well as antibacterial properties.[47] A wide variety of functional properties makes Ag-CPs useful for different applications. These properties include antibacterial activity,[47,53] gas sensing,[49] proton conductivity, high capacitance and good cycling ability,[54,55] and chemical sensing.[19,56] Moreover, Ag-CPs might play a significant role in environmental remediation,[57–59] as they have been tailored to achieve a particular mechanism of oxoanion exchange to maximize their effectiveness.[60] Most recently, there were several reports on Ag-CPs manifesting excellent catalytic and photocatalytic properties.[61–64] Environmentally friendly and recyclable Ag-CP with 9,10-anthraquinone-1,4-dicarboxylate acid catalyzed the reaction of the visible-light-driven aerobic oxidation of alkynes into 1,2-diketones under ambient conditions.[61] 1D Ag-CPs with N',N'-2,2-tetrakis(diphenylphosphanylmethyl)thiocarbohydrazide showed exceptional performance as a photocatalyst for degradation of organic dyes in water, while-generating higher photocurrent response than molecular complexes with the same ligand.[62] Nano-microstructured Ag-CPs offer performance at a level competitive with known semiconductors in photocatalytic water splitting and degradation of organic pollutants and dyes.[63] They exhibit a highly reactive valence band potential and could be readily recycled, maintaining high activity after four uses.

Two Ag-CPs constructed using Co-metalloligands act as recyclable heterogeneous catalysts for the A3–coupling reactions of aldehydes, secondary amines and alkynes,[64] where the relative position of substituted pyridyl ring affected both the resulting coordination polymer structures and their catalytic activity.

Luminescent CPs are of great interest since they have been employed in sensing (metal ions, solvents and explosives) and (bio)imaging.[65–68] Some of the investigated Ag-CPs showed potential for ion[19,21,56,59] and solvent[69] sensing. In that sense, the goal of our work is the preparation of novel Ag-CPs, characterization of their luminescent properties at both low and room temperature, and explanation of its origin using TD-DFT. For the preparation of Ag-CPs, we used thiomorpholine-4-carbonitrile (L) and aromatic polyoxoacids as co-ligands (trimesic acid, H_3BTC; pyromellitic acid, H_4BTEC and 5-sulfosalicylic acid, H_35SSA, Figure 1). L was chosen as a ligand since it belongs to the class of *bis*-monodentate ligands which are able to form Ag-CPs[70–72], although it has never been used for this purpose. On the other hand, selected co-ligands showed photoluminescent properties[73–75] and can easily form Ag-CPs[56,73,84,85,76–83] – photoluminescent in some cases.[76–83,85,86]

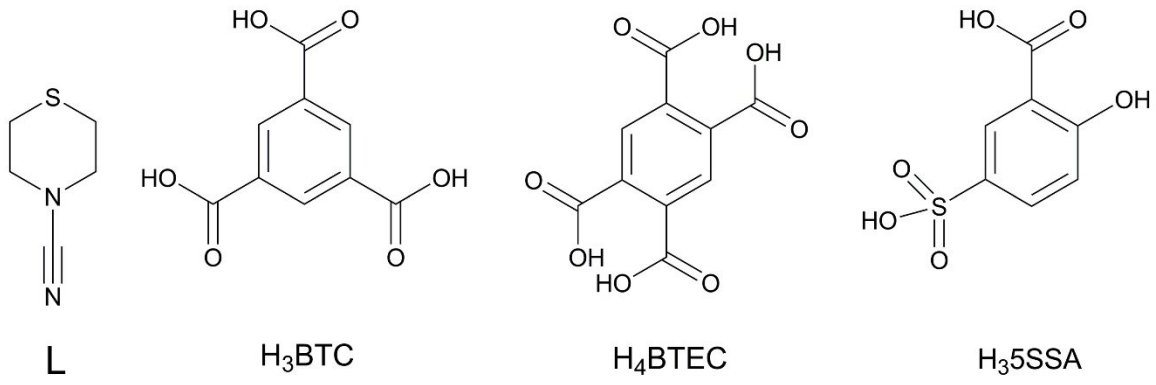

Figure 1. Structures of L and aromatic polyoxoacids co-ligands.

2. EXPERIMENTAL

2.1. Materials and methods

All the employed reagents and solvents were of analytical grade and used without further purification. $AgNO_3$ (≥ 99.0 %), $AgBF_4$ (98 %), 1,2,4,5-benzenetetracarboxylic acid (96 %) and 5-sulfosalicylic acid dihydrate (≥ 99.0 %) were obtained from Aldrich (Sigma-Aldrich Chemie GmbH, Steinheim, Germany). 1,3,5-benzenetricarboxylic acid (≥ 95.0 %) was obtained from Merck. Elemental analyses (C, H, N, S) were performed by the standard micro-methods using the ELEMENTARVario ELIII C.H.N.S=O analyzer. Infra-red (IR) spectra were recorded on a Thermo Scientific Nicolet 6700 FT-IR spectrometer by the Attenuated Total Reflection (ATR) technique in the region 4000−400 cm^{-1}. Abbreviations used for IR spectra: vs, very strong; s, strong; m, medium; w, weak. The NMR spectra were performed on a Bruker Avance 500 equipped with a broad-band direct probe.

2.2. Synthesis of the ligand thiomorpholine-4-carbonitrile (L)

The ligand was synthesized according to a modified literature procedure.[87] In a round bottom flask, thiomorpholine (1 equiv., 1 mmol), acetonitrile (0.5 M, 2 mL) and tetramethylethylenediamine (232 mg, 2 equiv., 2 mmol) were mixed together. Then CuCN (179 mg, 2 equiv., 2 mmol) was added and the mixture was flushed with oxygen. The reaction solution was then let to stir under 1 atmosphere of O_2 for 18 h. After a short filtration over Celite® that was rinsed thrice with AcOEt (3 × 3 mL), the crude mixture was concentrated under vacuum and purified by flash column chromatography (Pentane/AcOEt, SiO_2) to afford the entitled product. Yield 0.12 g (94%). White solid; m.p.: 41–43 °C. Anal. Calcd. for $C_5H_8N_2S$ (*MW* = 128.19): C, 46.85; H, 6.29; N, 21.85; S 25.01 %. Found: C, 46.65; H, 6.73; N, 21.74; S 25.12 %. ^{1}H NMR ($CDCl_3$, 500.26 MHz) δ_H: 2.70 (t, 4H), 3.46 (t, 4H); ^{13}C NMR ($CDCl_3$, 126 MHz) δ_C: 26.1, 50.8, 117.4.

2.3. Synthesis of {[Ag(L)$_2$](BF$_4$)}$_\infty$ (1)

A mixture of $AgBF_4$ (38.00 mg, 0.195 mmol) and L (50.00 mg, 0.393 mmol) dissolved in H_2O (5 ml) was placed in amber round bottom flask. Reaction mixture was refluxed for 1 h. Colorless single crystals suitable for X-ray diffraction analysis were obtained by slow evaporation and separated by filtration from colorless water solution. Yield: 0.017 g (19 %). Anal. Calcd. for

$C_{10}H_{16}AgBF_4N_4S_2$ (*FW* = 451.07): C, 26.63; H, 3.58; N, 12.42; S 14.22 %. Found: C, 27.04; H, 3.65; N, 12.80; S, 14.38 %. IR (ATR, ν_{max}/cm^{-1}): 3384 (w), 2998 (w), 2978 (w), 2928 (w), 2867 (w), 2225 (vs), 1446 (m), 1393 (m), 1343 (m), 1285 (m),1161 (m), 1098 (m), 1059 (s), 979 (m), 946 (m), 714 (w), 531 (w), 507 (w).

2.4. Synthesis of {[Ag(H_2BTC)(L)]×(H_3BTC)}$_\infty$ (2), {[Ag_2(H_2BTEC)(L)$_2$] × 3.33H_2O }$_\infty$ (3) and [Ag($H_2$5SSA)(L)]$_\infty$ (4)

A mixture of H_3BTC (82.00 mg, 0.390 mmol) in EtOH (5 ml), H_4BTEC (99.00 mg, 0.389 mmol) in MeOH (5 ml) or solid $H_3$5SSA (98.00 mg, 0.400 mmol) was added to the mixture of $AgNO_3$ (66.00 mg, 0.388 mmol) and L (50.00 mg, 0.393 mmol) in H_2O (10 ml) and placed in amber round bottom flask. Reaction mixture was refluxed for 1 h. White single crystals of **2** and pale-yellow single crystals of **3** and **4**, suitable for X-ray diffraction analysis, were obtained by slow evaporation and separated by filtration from colorless water solution.

2: Yield 0.058 g (29.5 %). Anal. Calcd. for $C_{23}H_{19}AgN_2O_{12}S$ (*FW* = 655.33): C, 42.15; H, 2.92; N, 4.27; S, 4.89 %. Found: C, 41.90; H, 2.90; N, 4.25; S, 4.95 %. IR (ATR, ν_{max}/cm^{-1}): 3128 (m), 2927 (m), 2650 (m), 2527 (m), 2227 (vs), 1694 (vs), 1607 (m), 1447 (s), 1393 (s), 1363 (s), 1282 (s), 1213 (s), 1157 (s), 1121 (s), 1031 (m), 982 (m), 943 (s), 739 (m), 698 (m), 675 (m), 656 (m), 532 (m), 509 (m).

3: Yield 0.146 g (68 %). Freshly prepared sample: Anal. Calcd. for $C_{20}H_{20}Ag_2N_4O_8S_2$×3.33$H_2O$ (*FW* = 784.31): C, 30.63; H, 3.43; N, 7.14; S, 8.18 %. Found: C, 30.70; H, 3.21; N, 7.27; S, 8.10 %. Sample dried in desiccator for seven days: Anal. Calcd. for $C_{20}H_{20}Ag_2N_4O_8S_2$ (*FW* = 724.26): C, 33.17; H, 2.78; N, 7.74; S, 8.85 %. Found: C, 33.05; H, 2.91; N, 7.57; S, 8.76 %. IR (ATR, ν_{max}/cm^{-1}; dried sample): 2931 (w), 2824 (w), 2511 (w), 2222 (s), 1822 (w), 1676 (vs), 1608 (s), 1490 (s), 1420 (s), 1378 (s), 1285 (s), 1169 (s), 1128 (s), 988 (s), 945 (s), 911 (s), 767 (s), 947 (m), 552 (m), 470 (w).

4: Yield 0.111 g (52 %). Anal. Calcd. for $C_{12}H_{13}AgN_2O_6S_2$ (*FW* = 453.23): C, 31.80; H, 2.89; N, 6.18; S, 14.15 %. Found: C, 31.52; H, 2.78; N, 6.12; S, 14.20 %. IR (ATR, ν_{max}/cm^{-1}): 3000 (w), 2793 (m), 2581 (w), 2500 (w), 2244 (m), 1666 (s), 1610 (m), 1179 (m), 1434 (m), 1370 (m), 1285 (m), 1233 (m), 1200 (m), 1166 (vs), 1118 (s), 1023 (s), 942 (m), 835 (w), 804 (w), 780 (w), 757 (w), 715 (w), 663 (w), 588 (s), 534 (w).

2.5. X- ray crystallography

X-ray diffraction data for **1–3** were collected at room temperature using Graphite-monochromated CuKα radiation (λ = 1.54184 Å) on an Oxford Diffraction Gemini S diffractometer. CrysAlisPro and CrysAlis RED software packages[88] were used for data collection and data integration. X-ray diffraction data for **4** were collected at 173 K on the Bruker APEX-II CCD diffractometer. Graphite-monochromated MoKα radiation (λ = 0.71073 Å) was used to measure diffraction from suitable single crystals of **4**. Bruker APEX2 and Bruker SAINT software packages[89] were used for data collection and data integration. Space group determinations for **1–4** were based on analysis of the Laue class and systematically absent reflections. Collected data for **1–3** were corrected for absorption effects using analytical numeric absorption correction applying a multifaceted crystal model,[90] while for **4** we used the multi-scan method, applying an empirical absorption correction using spherical harmonics as implemented in SADABS.[89] Structure solution and refinement for **1–4** were carried out with the programs SHELXT[91] and SHELXL-2018/3,[92] respectively. MERCURY[93] was employed for molecular graphics and WinGX[94] software was used to prepare material for publication. Non-hydrogen atoms were refined anisotropically while hydrogen atoms in **1** and **2** were treated by constrained isotropic refinement. On the other hand, hydrogen atoms in **3** and **4** were treated by a mixture of independent and constrained refinement. Even though complex **3** has disordered crystalline water molecules we presented its structure as it is, using SHELXL DFIX instructions to restrain O–H bond lengths. Crystal data and refinement parameters for **1–4** are summarized in Table 1. We also treated complex **3** by the SQUEEZE routine, implemented in Platon[95], to remove the disordered water molecules and presented crystal data and refinement parameters in Table S1 (Electronic supplementary material, ESI). Topological analysis was performed with the ToposPro program package and the TTD collection of periodic network topologies.[96]

Table 1. Crystallographic data and refinement parameters for **1–4**.

Crystal data				
Compound	**1**	**2**	**3**	**4**
Chemical formula	$2(C_5H_8Ag_{0.50}N_2S)\cdot BF_4$	$C_{23}H_{19}AgN_2O_{12}S$	$C_{30}H_{30}Ag_3N_6O_{12}S_3 \times 5H_2O$	$C_{12}H_{13}AgN_2O_6S_2$
FW	451.07	655.33	1176.47	453.23
Crystal system	Tetragonal	Triclinic	Monoclinic	Monoclinic
Space group	*P*–42$_1$*m*	*P*–1	*P*2$_1$/*n*	*P*2$_1$/*n*
a (Å)	13.1613 (6)	9.6126 (5)	9.8212 (10)	12.8066 (4)
b (Å)	13.1613 (6)	11.9927 (8)	26.3006 (4)	8.7191 (3)
c (Å)	4.4326 (6)	12.1218 (6)	16.2293 (3)	13.4239 (6)
α (°)	90	67.755 (6)	90	90
β (°)	90	78.686 (5)	93.666 (10)	97.048 (3)
γ (°)	90	68.517 (6)	90	90
V (Å^3)	767.81 (13)	1200.86 (14)	4183.51 (11)	1487.61 (10)
Z	2	2	4	4
D_x (Mg m^{-3})	1.951	1.812	1.868	2.024
μ (mm^{-1})	13.49	8.20	13.24	1.67
Crystal size (mm)	0.28 × 0.08 × 0.07	0.13 × 0.10 × 0.09	0.37 × 0.16 × 0.07	0.40 × 0.20 × 0.15
Data collection				
Absorption correction	Analytical	Analytical	Analytical	Multi-scan
T_{min}, T_{max}	0.178, 0.466	0.487, 0.606	0.094, 0.482	0.651, 0.746
Reflections collected	3187	7362	16229	29703
Independent reflections	799	4504	7963	5109
Observed reflections [$I > 2\sigma(I)$]	744	4022	6801	4548
R_{int}	0.034	0.025	0.026	0.018
Range of *h*, *k*, *l*	*h*=−16→13 *k*=−15→7 *l*=−5→4	*h*=−11→11 *k* =−14→14 *l*=−14→11	*h*=−12→11 *k*=−32→20 *l*=−19→19	*h*=−19→19 *k*=−12→12 *l*=−19→19
θ values (°)	θ_{max} = 72.8, θ_{min} = 4.8	θ_{max} = 72.6, θ_{min} = 4.0	θ_{max} = 71.7, θ_{min} = 3.2	θ_{max} = 32.0, θ_{min} = 2.1
Refinement				
$R[F^2 > 2\sigma(F^2)]$, $wR(F^2)$	0.0373, 0.0955	0.0326, 0.0828	0.0326, 0.0786	0.0222, 0.0525
R[*all data*], *wR*2	0.0410, 0.0998	0.0375, 0.0865	0.0393, 0.0823	0.0276, 0.0567
Goodness-of-fit (*S*)	1.058	1.025	1.031	1.086
No. of reflections	799	4504	7963	5109
No. of parameters	59	357	574	216
No. of restraints	0	0	136	0
$\Delta\rho_{max}$, $\Delta\rho_{min}$ (e Å^{-3})	0.48, −0.39	0.48, −0.39	0.76, −0.73	0.52, −0.51
CCDC no.	1987944	1987947	1990303	1987949

The X-ray powder diffraction experiment was conducted on Rigaku Smartlab X-ray diffractometer in θ-θ geometry (the sample in horizontal position) in parafocusing Bragg-Brentano geometry using D/teX Ultra 250 strip detector in 1D standard mode with $CuK_{\alpha 1,2}$ radiation source (U = 40 kV and I = 30 mA). The XRPD patterns were collected in 5-65° 2θ range, with a step of 0.01°, and the data collection speed of 5 °/min with horizontal sample rotation of 20 rpm. For every compound, a small amount of single-crystal sample was pulverized, and low background single crystal silicon sample holder was used to minimize the background. The crystal phases present in the samples were identified in dedicated Rigaku PDXL 2.0 software, comparing them with user database comprised of CIFs previously obtained by a single crystal X-ray diffraction.

2.6. Hirshfeld surface analysis and intermolecular interaction energies

Hirshfeld surface analysis was carried out using the Crystallographic Information File. Before calculating the surfaces, the lengths of the bonds which include hydrogen atoms were normalized to standard values determined by neutron diffraction. The Hirshfeld surfaces visualization and the presentation of the results as d_{norm}, shape index, and curvedness, as well as the calculation of 2D fingerprint plots with d_e and d_i distances were pefrormed by Crystal Explorer v.17.5.[97,98] The parameter d_{norm} represents the sum of the distance of the nearest nucleus external to the surface (d_e) and the distance from the surface to the nearest nucleus internal to the surface (d_i), normalized by the van der Waals radius of the atom. The surfaces were mapped over a standard color scale, with the corresponding 2D fingerprint plots calculated using d_e and d_i values in the range 0.4–2.8 Å. The intermolecular interaction energies were determined using CrystalExplorer v17.5, with the wavefunction calculated using Gaussian09 software[99] with B3LYP method and DGDZVP basis set.[100] The model systems were built from supercells of different size by creating a non-polymeric system. This was achieved by removing the metal centers, preserving whole ligand molecules, and capping eliminated covalent bonds with hydrogen atoms to preserve the charge balance.

2.7. TGA-DSC analysis

Thermal data were collected using the TA Instruments SDT Q600 thermal analyzer. The decomposition was followed from room temperature to 400 °C at 10 °C min^{-1} heating rate in argon carrier gas (flow rate = 30 cm^3 min^{-1}). Sample holder/reference is alumina crucible/empty alumina crucible. The sample mass was 3–5 mg.

2.8. Photocatalytic and photophysical properties

Mordant blue (MB9), a widespread environmental pollutant, is a commonly used dye in the textile industry. A volume of 50 ml of dye solution in water (c = 0.5 mol/L), was mixed with 50 mg of each of the complexes. The powdered complexes were added to the water solution under constant stirring and left in the dark for 15 min to equilibrate. The samples were illuminated by a spotlight source (Hamamatsu LC5) from a distance of 1 cm (light intensity 5.2 mW/cm^2). The decomposition rate of MB9 as a function of irradiation time was measured by a Varian Cary 50 Scan UV-Vis spectrophotometer. A lamp with the emission in the UV and visible part of the spectrum was turned on, followed by the extraction of 5 ml of solution at regular intervals later measured in a UV/VIS spectrometer. MB9 has two main absorption regions: around 330 and around 530 nm. The relative concentration of MB9 is tracked using absorption intensities in these regions. The measured absorption intensities were used to calculate relative concentrations of MB9 dye and the corresponding rate constants for the photocatalytic degradation reaction of MB9 dye.[101]

Diffuse reflectance UV-vis spectra of pressed powder samples diluted with KBr were recorded on a Shimadzu (UV-3600 spectrophotometer with a Harrick Praying Mantis accessory) and recalculated following the Kubelka−Munk function. Excitation and emission spectra in the solid state were recorded with a Jobin-Yvon Horiba Fluorolog 3–22 Tau-3 spectrofluorimeter. Lifetime measurements were recorded with a Datastation HUB-B with a nanoLED controller and DAS6 software. The nanoLED employed for lifetime measurements were of 320 nm with pulse lengths of 0.8–1.4 ns. The lifetime data were fitted with the Jobin-Yvon software package.

2.9. Computational details

Single point DFT and TD-DFT calculations were carried out for models **3** and **4**. In both the ground-state calculations and the subsequent calculations of the electronic excitation spectra, the B3LYP functional[102–104] as implemented in TURBOMOLE[105] was used. The excitation energies were obtained at the density functional level by using the time dependent perturbation theory approach (TD-DFT),[106–109] which is a DFT generalization of the Hartree-Fock linear response (HF-LR) or random-phase approximation (RPA) method.[110] In all calculations, the Karlsruhe split-valence quality basis sets augmented with polarization functions[111,112] were used for the light elements (SVP) whereas the def2-TZVP bases sets were used for Ag.[113] The Stuttgart effective core potential in TURBOMOLE was used for Ag.[114]

3. RESULTS AND DISCUSSION

3.1 Molecular and crystal structures of 1–4

Complex **1** crystallizes in the tetragonal $P\text{–}42_1m$ space group. The asymmetric unit of **1** contains a Ag(I) and a tetrafluoroborate anion, both of a quarter occupancy, as well as a half of the L ligand. Ag(I) atoms are situated on a 2-fold axis along which two mirror planes intersect (Wyckoff position 2*c*, site symmetry 2.mm). Moreover, L lies on the (110) mirror plane (Wyckoff position 4*e*, site symmetry ..m) with half-occupancy, except for the C2 and C3 atoms in general positions. The F1 atom of the tetrafluoroborate anion is in a general position, while the quarter-occupancy B1 atom is located at the Wyckoff 2*a* position (site symmetry –4..). The part of infinite structure of **1** depicted in Figure 2A shows that Ls form a distorted tetrahedron around the Ag(I). The geometric index of distortion is $\tau_4 = 0.86$.[115] Each of the Ag(I) ions in **1** is coordinated to two nitrogen and two sulfur atoms from four different L ligands. Selected bond lengths are given in Table 2. L acts as a bridging ligand with *bis*–monodentate coordination connecting the Ag(I) ions to form a two-dimensional coordination network (Figure 2B). The crystal packing of **1** comprises of 2D layers stacked along *c*-axis with a thickness of 4.57 Å (Figure 2C).

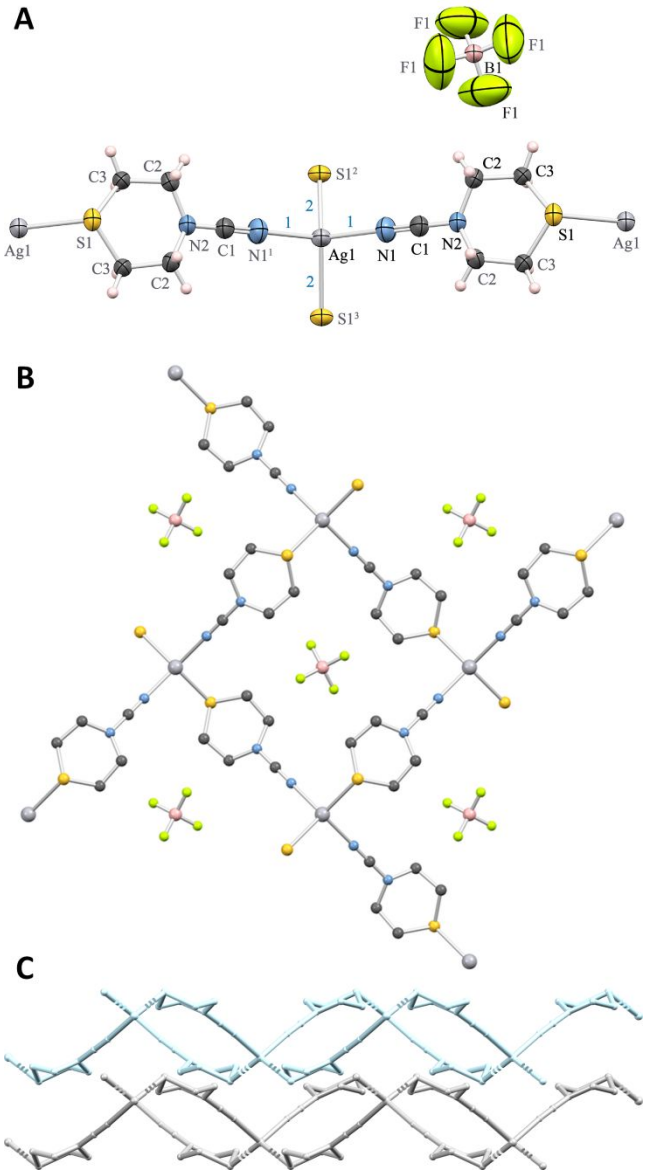

Figure 2. (A) ORTEP drawing (generated by MERCURY[93]) of the part of infinite structure of **1** with labeled non-H atoms. The atoms of the asymmetric unit are labeled in black. Displacement ellipsoids are shown at the 50% probability level, while the H atoms are drawn as spheres of arbitrary radii. Symmetry codes: (1) $-x+1, -y, z$; (2) $y, -x+1, -z$; (3) $-y+1, x-1, -z$. Lengths of bonds labeled as 1 and 2 (in blue) are given in Table 2. (B) The crystal packing of **1** viewed along *c*-axis. (C) Stacked layers viewed along *b*-axis. All hydrogen atoms (B, C) and tetrafluoroborate anions (C) are omitted for clarity.

Table 2. Selected bond lengths for **1**–**4**.

Compound	Bond label	Bond type	Bond length (Å)
1	1	Ag1–N1, Ag1–N1[1]	2.327(9)
	2	Ag1–S1[2], Ag1–S1[3]	2.555(2)
2	3	Ag1–N1	2.180(3)
	4	Ag1–S1[9]	2.4164(7)
	5	Ag1–O1	2.406(2)
3	6	Ag1–N1	2.221(3)
	7	Ag1–O1	2.340(2)
	8	Ag1–S3[11]	2.4309(11)
	9	Ag1–O5[12]	2.479(3)
	10	Ag2–N2	2.245(3)
	11	Ag2–O5	2.333(2)
	12	Ag2–S1[13]	2.4321(10)
	13	Ag2–O1[14]	2.467(3)
	14	Ag3–N3	2.216(3)
	15	Ag3–O9	2.343(2)
	16	Ag3—S2	2.4341(11)
	17	Ag3–O9[15]	2.494(3)
4	18	Ag1–N1	2.1818(15)
	19	Ag1–O1	2.4576(11)
	20	Ag1–S1	2.4903(4)
	21	Ag1–O2	2.6170(1)

Symmetry codes: (1) −*x*+1, −*y*, *z*; (2) *y*, −*x*+1, −*z*; (3) −*y*+1, *x*−1, −*z*; (9) *x*−1, *y*, *z*; (11) −*x*+2, −*y*+1, −*z*+1; (12) −*x*+1, −*y*+2, −*z*+1; (13) −*x*+1, −*y*+1, −*z*+1; (14) *x*+1, *y*, *z*; (v) *x*+1/2, −*y*+3/2, *z*+1/2; (15) *x*−1/2, −*y*+3/2, *z*−1/2.

Complex **2** crystallizes in the triclinic *P*–1 space group. The asymmetric unit consists of a Ag(I) ion, one of each L and H_2BTC^- ligands, as well as one neutral non-coordinated H_3BTC molecule. The part of infinite structure of **2**, shown in Figure 3A, reveals that the Ag(I) ion tri-coordinated by a nitrogen and a sulfur atom from two different L ligands and one deprotonated carboxylate oxygen atom from H_2BTC^-. This gives rise to a distorted trigonal planar geometry with values of N1–Ag1–O1, N1–Ag1–S1[9], and O1–Ag1–S1[9] angles of 93.77(12)°, 149.25(11)°,

and 116.24(6)°, respectively. Selected bond lengths are given in Table 2. The coordination mode of H_2BTC^- is monodentate, while L behaves as a *bis*-monodentate ligand creating a centrosymmetric 1D chain parallel to the *a*-axis (Figure 3B). Non-coordinated H_3BTC molecule and H_2BTC^- ligands are connected by the O–H···O hydrogen interactions (Table 3).

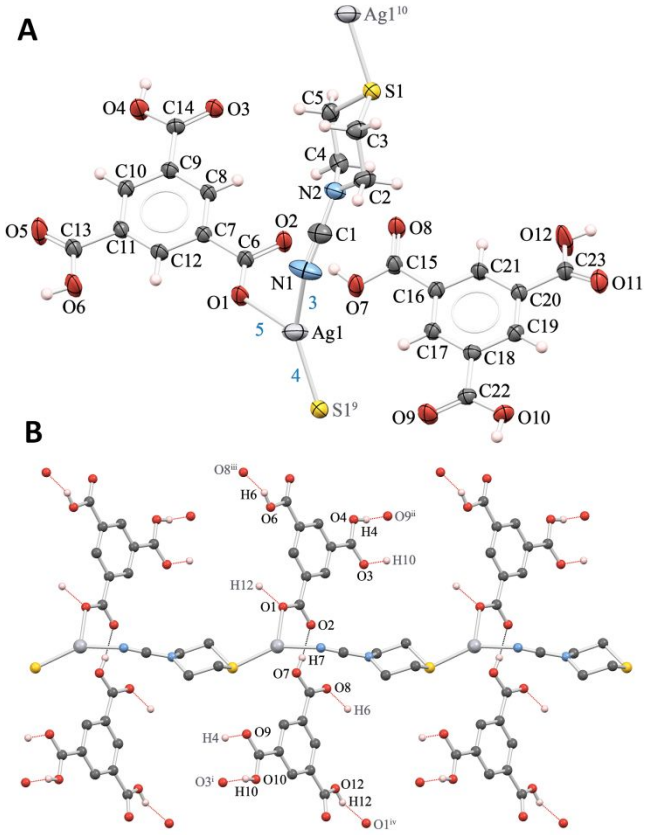

Figure 3. (A) ORTEP drawing (generated by MERCURY[93]) of the part of infinite structure of **2** with labeled non-H atoms. The atoms of the asymmetric unit are labeled in black. Displacement ellipsoids are shown at the 50% probability level, while the H atoms are drawn as spheres of arbitrary radii. Symmetry codes: (9) $x-1, y, z$; (10) $x+1, y, z$. Lengths of bonds labeled as 3–5 (in blue) are given in Table 2. (B) The crystal packing of **2** viewed along *c*-axis. Selected hydrogen bonds are showed as dashed lines. The hydrogen atoms not involved in the selected hydrogen bonds are omitted for clarity.

Table 3. Selected hydrogen bond parameters in the crystal packing of **2**.

D–H···A	D–H (Å)	H···A (Å)	D···A (Å)	D–H···A (°)
O10—H10···O3^{i}	0.82	1.82	2.638 (3)	172.8
O7—H7···O2	0.82	1.70	2.517 (3)	171.0
O4—H4···O9^{ii}	0.82	1.81	2.613 (3)	166.5
O6—H6···O8^{iii}	0.82	1.95	2.698 (3)	151.9
O12—H12···O1^{iv}	0.82	1.82	2.601 (3)	158.5

Symmetry codes: (i) $x-1, y+1, z-1$; (ii) $x+1, y-1, z+1$; (iii) $x, y-1, z$; (iv) $x, y+1, z$

Complex **3** crystallizes in the monoclinic $P2_1/n$ space group. The asymmetric unit contains three crystallographically different Ag(I) ions, three L ligands, one and a half H_2BTEC^{2-} ligand and five disordered water molecules. Each Ag(I) ion is coordinated to one sulfur and one nitrogen atom from different L ligands, as well as two deprotonated carboxylate oxygen atoms from different H_2BTEC^{2-} ligands. Selected bond lengths are given in Table 2. The coordination mode of L is *bis*-monodentate, while H_2BTEC^{2-} behaves as a *bis*-bidentate bridging ligand. The part of infinite structure is depicted in Figure 4A. The geometry around each of the Ag(I) ions is distorted tetrahedral with the geometric index of distortion of $\tau_4 = 0.70$ (Ag1), $\tau_4 = 0.76$ (Ag2), and $\tau_4 = 0.74$ (Ag3), thus the structure at each Ag(I) in **3** can be described as seesaw.[115] The crystal packing comprises of 2D layers of 5.83 Å thickness parallel to the (110) plane (Figure 4 B,C). A CSD[116] search performed by Con-Quest 1.18[93] showed that **3** is the first compound containing H_2BTEC^{2-} ligand coordinated to Ag(I).

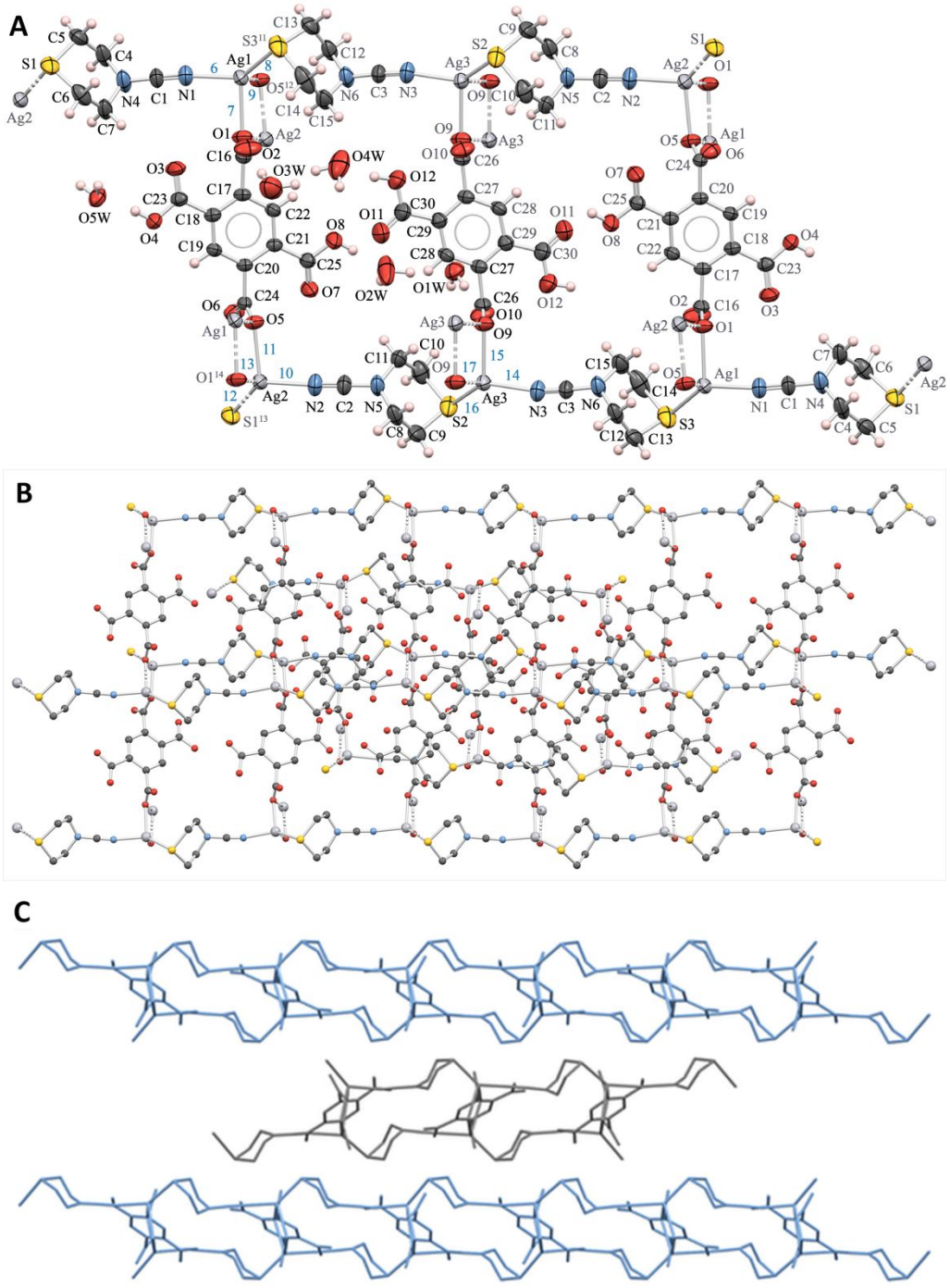

Figure 4. (A) ORTEP drawing (generated by MERCURY[93]) of the part of infinite structure of **3** with labeled non-H atoms. The atoms of the asymmetric unit cell are labeled in bold. Displacement ellipsoids are shown at the 50% probability level, while the H atoms are drawn as spheres of arbitrary radii. Lengths of bonds labeled as 6–17 (in blue) are given in Table 2. (B)

The extended structure of **3** viewed parallel to *c*-axis. (C) The extended structure of **3** viewed along *a*-axis showing two-dimensional layers. All hydrogen atoms are omitted for clarity (B, C).

Complex **4** crystallizes in the monoclinic $P2_1/n$ space group. The asymmetric unit consists of a single Ag(I) atom and one of each L and H_25SSA^- ligands. Two sulfonate oxygen atoms from two different H_25SSA^- ligands are coordinated to Ag(I), as well as a nitrogen and a sulfur atom from two different L ligands. The part of the infinite structure is illustrated in Figure 5A. As τ_4 = 0.75, the geometry around each of the Ag(I) atoms is seesaw.[115] Selected bond lengths are given in Table 2. Both H_25SSA^- and L behave as *bis*-monodentate ligands, with L creating a centrosymmetric double 1D chain parallel to *b*-axis. (Figure 5B). The crystal packing is based on H-interactions (Table 4). A CSD[116] search performed by Con-Quest 1.18[93] showed that **4** is the first compound containing H_25SSA^- ligand coordinated to Ag(I).

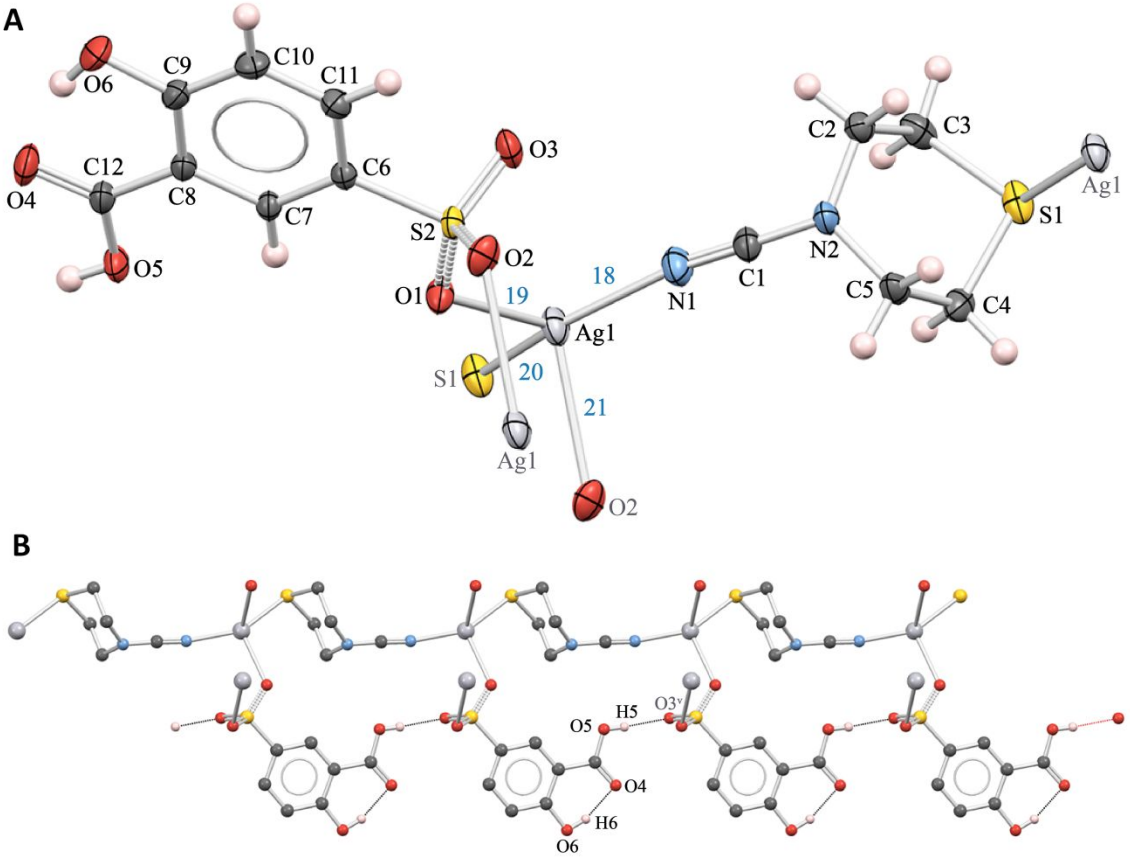

Figure 5. (A) ORTEP drawings (generated by MERCURY[93]) of the part of infinite structure of **4** with labeled non-H atoms. The atoms of the asymmetric unit cell are labeled in black.

Displacement ellipsoids are shown at the 50% probability level, while the H atoms are drawn as spheres of arbitrary radii. Lengths of bonds labeled as 18–21 (in blue) are given in Table 2. (B) The crystal packing of **4** viewed along *c*-axis. Selected hydrogen bonds are showed as dashed lines. The hydrogen atoms not involved in the selected hydrogen bonds are omitted for clarity.

Table 4. Selected H-bond parameters in the crystal packing of **4**.

D–H···A	D–H (Å)	H···A (Å)	D···A (Å)	D–H···A (°)
O5—H5···O3^{v}	0.80 (3)	1.82 (3)	2.6246 (17)	175 (3)
O6—H6···O4	0.85 (3)	1.76 (3)	2.575 (2)	162 (3)

Symmetry code: (v) *x*, *y*+1, *z*

Topological analysis in standard representation suggests that each Ag(I) in **1** and **4** acts as a 4-connected node. The overall structure of **1** has a **sql**, while **4** has (4,4)(0,2) underlying net topology.[117] In contrast, each Ag(I) ion in **2** acts as a 2-connected node with 2C1 underlying net topology. [117] The structure of **3** can be described as a binodal net. Both Ag(I) ions and H_2BTEC^{2-} ligands act as 4-connected nodes, giving rise to a **4,4L28** underlying net topology.[117]

All samples correspond to the single-phase X-ray powder patterns (Figure S1, ESI) in accordance with the structural model obtained by the single-crystal X-ray diffraction.

3.2. ***Hirshfeld and 2D fingerprint plot analysis***

Visualization and quick and easy understanding of intra- and intermolecular interactions in the crystal structures can be achieved using Hirshfeld surface and fingerprint plot analysis.[97,118] The Hirshfeld surfaces and the pseudosymmetric 2D fingerprint plots,[119] as well as the existing classical and non-classical interactions in the crystal structures of **1**–**4** are depicted in Figure 6. In all complexes, interactions can be observed in the shape-index plot as red and blue regions, as well as in the curvature plot as a flat zone in the same position of the surface as

in the shape-index plot. White circles mark the regions of the surfaces through which the complexes interact.

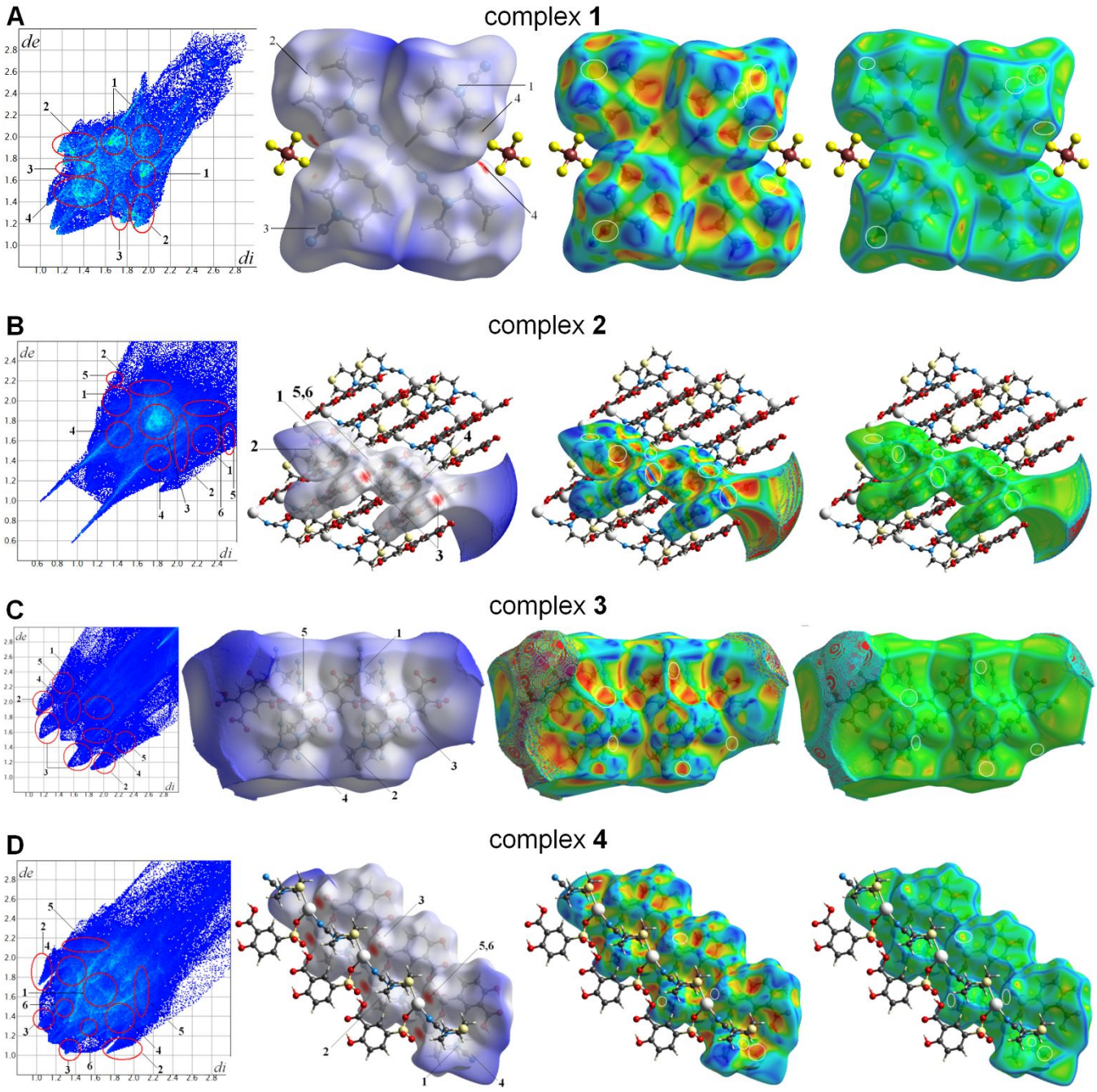

Figure 6. 2D fingerprint plot, Hirshfeld surface mapped with d_{norm}, shape index and curvedness for **1**–**4**. For interaction types see Table 4.

The relative contributions of different types of interactions in **1**–**4** are shown in Table 5. As expected, the O···H interactions are completely absent in **1** since it does not contain any co-ligand, and therefore no oxygen. On the other hand, the O···H interactions are the most dominant type in other three complexes with aromatic polyoxoacids acids as co-ligands. Furthermore, **2** exhibits uncommonly high contribution of interactions of hydrogen and oxygen with the metal center. This can be attributed to proximity of the carboxylic group of the tricarboxylic acid to the metal (at 2.9 Å and 3.2 Å), which is just slightly longer than the Ag–O distance of the coordinated carboxylic group (2.4 Å). This indicates particularly strong interactions of the metal center with the carboxylic groups perpendicular to the plane of coordination, resulting in a quasi-3D structure for **2**, with 2D planes connected through the strong Ag···O interactions on the perpendicular axis. This type of interaction is also present in **4**, where the Ag···O distances are 2.6 and 3.4 Å, and the interaction comes primarily from the oxygen atoms bound to the sulfur. Absence of the Ag···O interactions in **3** can be correlated with the tetrahedral coordination around the metal.

Table 5. Relative contributions (in %) and ($d_i + d_e$) values (in Å) of different interaction types in the crystal structures of **1–4**.

		1		**2**		**3**		**4**	
Interaction number	interaction type	relative contribution	$d_i + d_e$	relative contribution	$d_i + d_e$	relative contribution	$d_i + d_e$	relative contribution	$d_i + d_e$
1	N···H	6.4	2.9	2.3	2.2	7.55	3.6	3.45	3.2
2	S···H	3.5	3.0	0.75	2.3	2.35	3.6	2.0	3.4
3	C···H	3.85	-	2.1	-	1.65	-	8.65	-
4	F···H	4.85	2.5	-	-	-	-	-	-
4’	O···H	-	-	13.6	1.2	17	3.0	12.1	2.6
5	Ag···H	-	-	8.3	2.4	0.45	-	1.3	2.2
6	Ag···O	-	-	5.9	2.6	-	-	2.25	2.4

3.3. Intermolecular interactions

Different types of intermolecular interactions within the crystal packing play an important part in the behavior of co-crystals, affecting their photophysical and pharmaceutical properties.[120] Table 6 shows an overview of the calculated values of intermolecular interactions

in model systems for all four complexes. These values are in a similar range for all systems – around 40 kJ/mol per monomer unit. However, the relative contributions of different types of interactions vary from one system to another (Tables S2–S5, ESI). In **1**, the intermolecular interactions are absolutely dominated by the dispersion interactions (88% contribution of attractive interactions, Table 7), while the electron interactions are almost negligible. This can be attributed to the stacking of monomer units in 2D layers. In **2**, on the other hand, electron interactions are more dominant (49% contribution to attractive interactions, Table 7), with dispersion playing an important part. In **3** and **4**, the dispersion interactions contribute 48% and 55% (Table 7), respectively, while the electron interactions contribute 35% and 31%, respectively, to the attractive interactions. This can be attributed to the increased role of hydrogen bonding, particularly between oxygen and hydrogen, in **2**–**4**. In addition, **2** exhibits the highest contribution of interactions between hydrogen and metal center, which can be correlated with its highest contribution of electron interactions. In all complexes, polarizations interactions contribute 11–17% (Table 7) to the overall attractive interaction energy, indicating that different composition and structure has relatively little effect on the role of this type of interactions. In **3**, slightly increased contribution of polarization interactions can be correlated with somewhat lower overall energy of intermolecular interactions. Differences in contributions of different types of interactions can be correlated to the spatial arrangement of monomer units in the lattice, with the location and orientation of hydrogen bonding being the decisive contributor to the electronic contribution to the value of the energy of attractive interactions. The negligible contribution of the electron interactions in **1** can be attributed largely to the absence of oxygen in the structure.

Table 6. Overview of calculated values for intermolecular interactions in model systems of **1**–**4**.

Complex	Intermolecular Interactions (kJ/mol)	monomer units	Per monomer unit (kJ/mol)
1	–84.6	2	–42.3
2	–682.2	16	–42.64
3	–288.3	8	–36.04
4	–466.9	12	–38.91

Table 7. Relative contributions (in %) to attractive interactions in the crystal structures of **1**–**4**.

Complex	Electron	Polarization	Dispersion
1	0.5	11.1	88.4
2	48.6	13.8	37.6
3	35.2	17.0	47.8
4	30.9	14.0	55.1

3.4. Thermal properties of 1–4

Based on the thermoanalytical data, **1–4** do not contain any lattice solvents. Complex **3** crystallizes with 3.33 water molecules per formula unit (Table 1). However, the lattice water almost completely evaporates during storage in desiccator for seven days. The thermal stability of the compounds, given by their onset temperatures, is relatively high and increases as follows: 173 °C (**3**) < 188 °C (**4**) < 192 °C (**1**) < 237 °C (**2**). The decomposition mechanism of each CP is different, in accordance with their different composition and structure. In all cases, the decomposition is a complex process which occurs in several more or less overlapped steps (Figure 7A).

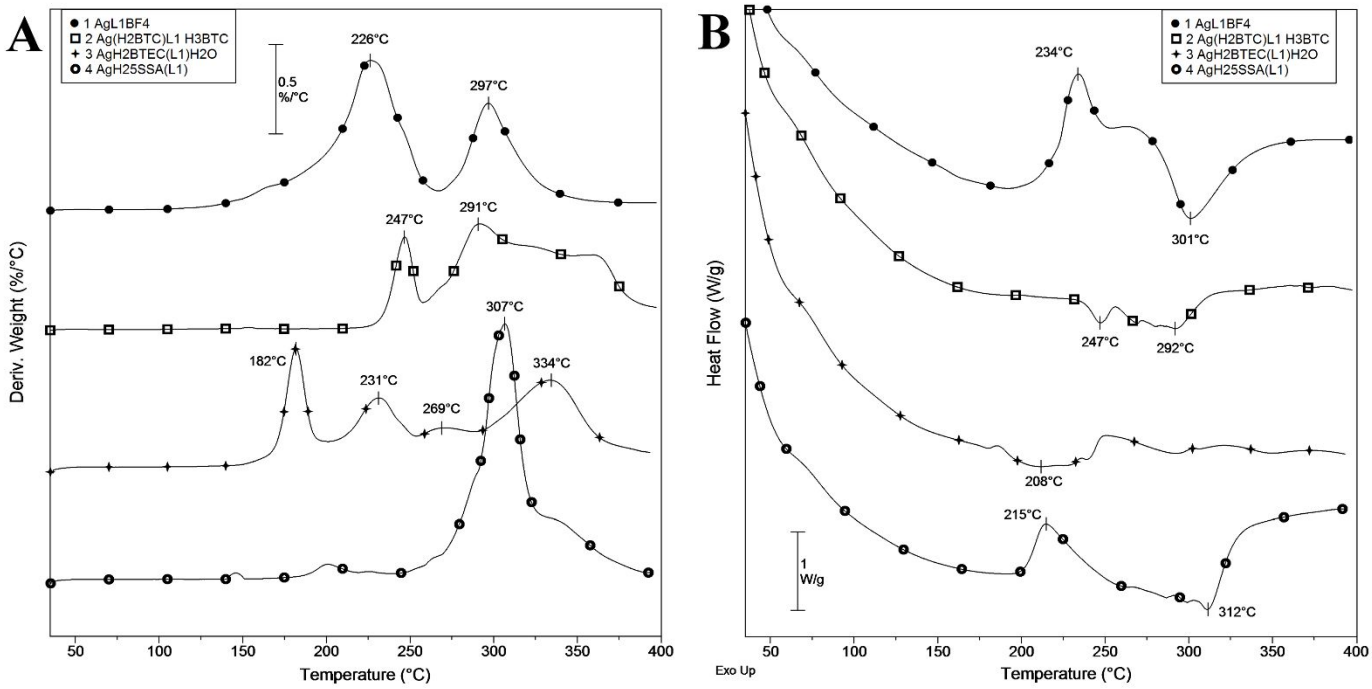

Figure 7. DTG (A) and DSC (B) curves of **1–4** in argon.

The simultaneously recorded DSC curves are shown in Figure 7B. As can be seen, the decomposition of **1** and **4** begins with an exothermic process. Although the thermal decomposition of tetrafluoroborates in most cases is followed by endothermic heat effects,[121–123] in this case, the decomposition is exothermic. This phenomenon may be a result of intramolecular redox reactions between Ag^+ and L which are less pronounced in **2**–**4**, most likely because of the nature of the co-ligands. Additionally, **1** is cationic complex with BF_4^- as counter ion, and all other complexes contain the organic co-ligands coordinated to Ag(I). The oxidative properties of Ag^+ in the presence of BF_4^- are discussed in the literature.[124] The small mass loss of **4** at ~200°C, followed by exothermic heat effect is most probably a CO_2 releasing process in accordance with the composition of the compound. Above ~250 °C the thermal decomposition of **4** continues with endothermic processes (Figure 7B). The decomposition process of **2** and **3** is followed by endothermic effects in the whole temperature range of analysis (Figure 7B).

3.5. Photocatalytic properties

Photocatalytic properties of **1**–**4** were investigated in the reaction of photocatalytic degradation of MB9 dye. Since all complexes are insoluble in water, they were tested as heterogeneous catalysts in powder form for a degradation reaction in water. The progress of degradation reaction was monitored using UV/VIS spectroscopy (Figure S2, ESI) and the results are shown in Table 8. A dependence of $-\ln(C/C_0)$ on time (Figure S3, ESI), where the initial part of the curve shows linear dependence (with $R^2 > 99\%$) in all four complexes, indicates that the reaction of the photocatalytic degradation of MB9 dye can be treated as a first-order reaction. Apparent first-order rate constants for all four compounds were calculated to be in 0.036–0.056 min^{-1} range, which is comparable to the values obtained for ZnO-based photocatalysts in photocatalytic degradation of organic dyes.[125] In addition, this is also comparable to or better than the reported activities for Ag-based CPs for photocatalytic degradation of organic dyes[126–129]. This indicates that all four complexes exhibit reasonably high photocatalytic activity. The lowest value was obtained for **1**, and the highest for **2**. It is interesting to note that **3** has more Ag atoms per monomer unit (Table 8) than **1, 2** and **4**, therefore, the increase in photocatalytic activity cannot be attributed to higher Ag content. There is also no significant difference in the accessible free lattice volume for water (all four complexes have 0), suggesting that none of the structures exhibits porosity. Therefore, the increase in photocatalytic activity can most likely be correlated with the existence of different co-ligands in the four complexes: **1** does not contain carboxylic acid as a co-ligand and exhibits the lowest photocatalytic activity, **4** contains $H_3$5SSA and exhibits lower photocatalytic activity than **3** and **2**, which contain H_4BTEC and H_3BTC, respectively. Complex **2** also contains free H_3BTC molecule in addition to the one coordinated to the metal center. Complex **4** contains one carboxylic group and one hydroxyl group in addition to sulfonic acid group, **3** contains one tetracarboxylic acid, while **2** contains two tricarboxylic acids. This suggests that the photocatalytic mechanism most likely includes active hydroxyl radicals (•OH) as the main reactive species.[126,127] The excited state of the complex reacts with water to form •OH which oxidizes the dye. The oxygen in the system can easily re-oxidize the reduced complex species making it active again. The presence of more reactive carboxylic groups in the system enhances the photocatalytic activity of the complexes, and the change photocatalytic reactivity of these complexes can be roughly correlated with increasing number of oxygen groups in the structure.

Table 8. Calculated apparent first-order rate constants corresponding to each compound

Compound	General formula	Empirical formula (*FW*)	Rate constant (min^{-1})
1	$\{[Ag(L)_2](BF_4)\}_\infty$	$C_{10}H_{16}AgBF_4N_4S_2$ (*FW* = 451.07)	0.036±0.001
2	$\{[Ag(H_2BTC)(L)]\times(H_3BTC)\}_\infty$	$C_{23}H_{19}AgN_2O_{12}S$ (*FW* = 655.33)	0.056±0.003
3	$\{[Ag_2(H_2BTEC)(L)_2]\}_\infty$	$C_{20}H_{20}Ag_2N_4O_8S_2$ (*FW* = 724.26)	0.055±0.004
4	$[Ag(H_25SSA)(L)]_\infty$	$C_{12}H_{13}AgN_2O_6S_2$ (*FW* = 453.23)	0.040±0.002

3.6. Photophysical properties

While complexes **1** and **2** do not show emissive properties in the solid state at RT or 77 K, complexes **3** and **4** display luminescent emissions in the solid state when they are irradiated with UV light. Complex **3** is not luminescent at RT, but it is luminescent at 77 K, showing an emission band centred at 522 nm (λ_{exc} 340 nm). In contrast, **4** is emissive at RT, displaying a more energetic emission located at 430 nm (λ_{exc} 330 nm). When the temperature is decreased to 77 K, a very similar emission, without any noticeable energetic shift, is detected for this complex (Figure 8).

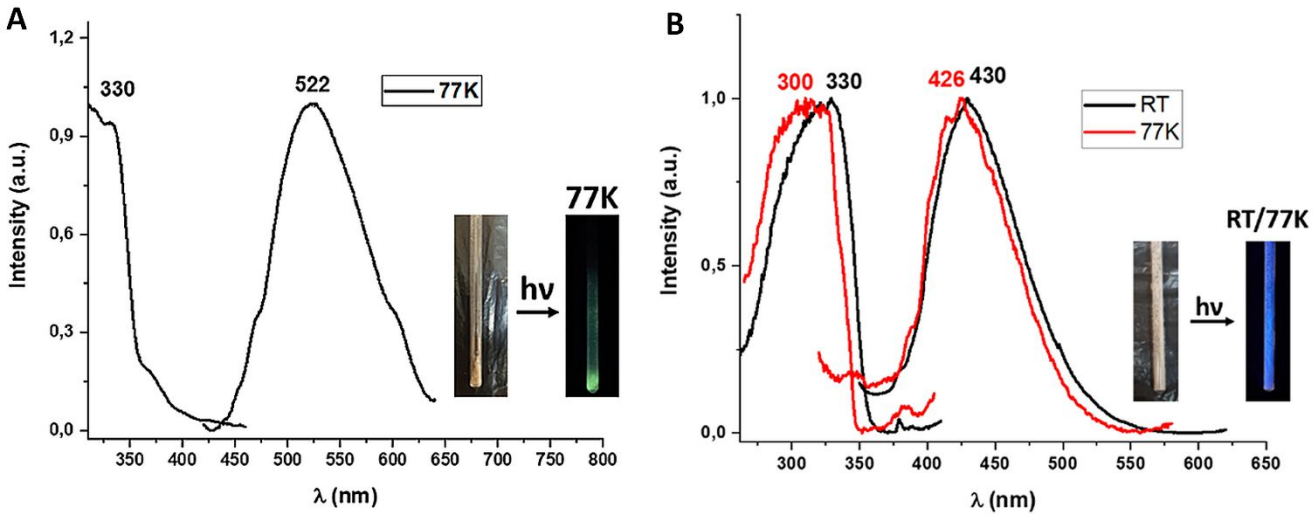

Figure 8. Excitation and emission spectra in solid state at 77K (A) and room temperature and 77 K (B) for **3** and **4,** respectively.

The lifetime obtained for the emission for **3** at 77 K is 8 ns, while for **4** it is 7 and 8 ns at room temperature and 77 K, respectively. These lifetimes seem to indicate electronic transitions of singlet parentage for the origin of the experimentally observed emissions. In fact, the excitation spectra collected in the solid state for **3** and **4** appear included within the wavelength range of the corresponding absorption spectra in the solid state, suggesting that the transitions are allowed and, therefore, related to fluorescence processes for both complexes (Figure 9).

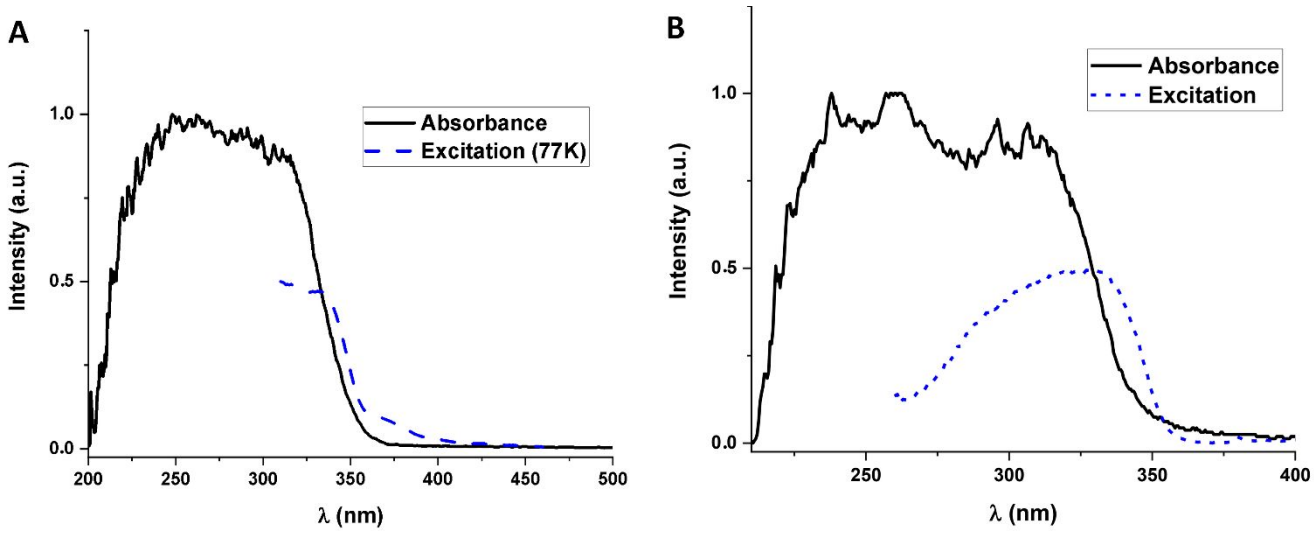

Figure 9. Absorbance (black) and excitation (blue) spectra in the solid state for **3** (A) and **4** (B).

3.7. Computational studies

DFT and TD-DFT computational calculations were carried out to elucidate the origin of the luminescent properties displayed by **3** and **4**. Tetranuclear model systems were constructed based on the experimental X-ray diffraction data, keeping all the distances and the angles fixed and representing all the bonds and interactions found in the coordination polymers (Figure 10).

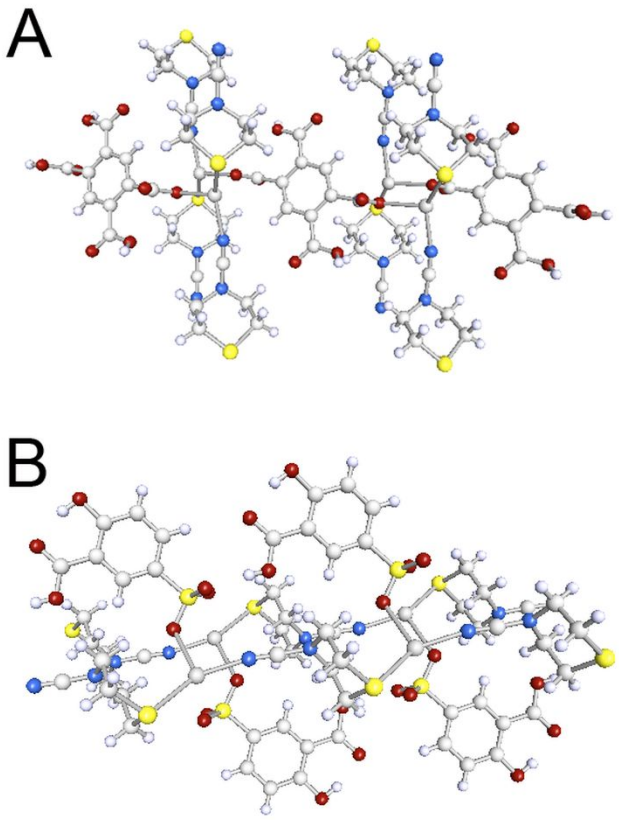

Figure 10. Theoretical model systems representing complex **3** (A) and **4** (B).

Single point DFT calculations permit the analysis of the electronic structure for these complexes. Figures 11 and 12 display the most important frontier molecular orbitals (MOs) as computed.

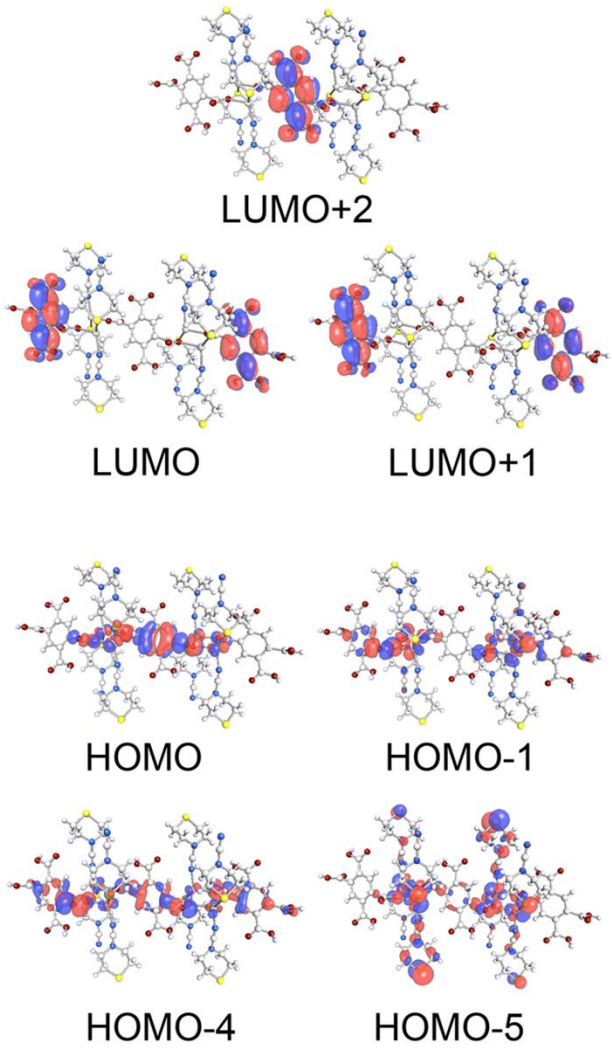

Figure 11. Frontier MOs for model system **3**

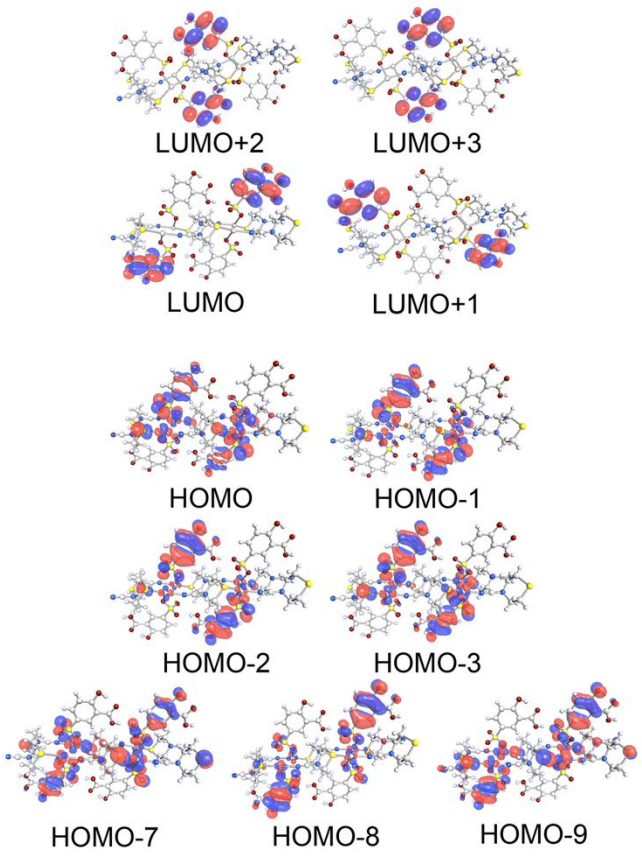

Figure 12. Frontier MOs for model system **4**.

If we analyse the results obtained for the electronic structure for model **3**, we observe that HOMO, HOMO-1 and HOMO-4 orbitals are located mostly at the H_2BTEC^{2-} ligand (aromatic ring and carboxylate groups), with some contribution from the Ag centres. Meanwhile, HOMO-5 ligand is mostly located at L with a minor contribution from the Ag centres. On the other hand, the lowest unoccupied orbitals LUMO to LUMO+2 appear to be located mostly at the H_2BTEC^{2-} ligands, without contribution from the Ag centres. In the case of model system **4**, similar behaviour is computed. Thus, the molecular orbitals from HOMO to HOMO-9 appear mostly centred on the aromatic ring and the SO_3 functional group of the H_25SAA^- ligands with a minor contribution from the Ag atoms bonded to the SO_3 groups. Regarding lowest occupied molecular orbitals, from LUMO to LUMO+3 are located on the aromatic ring of the H_25SAA^- ligands with minor contributions from the COOH and OH groups bonded to the aromatic ring of the ligand. In these empty orbitals, the participation of the Ag atoms or the L ligands is, again, not detected.

The TD-DFT computation of the first 25 singlet-singlet electronic excitations provides same information on the origin of the fluorescent properties of **3** and **4**. Table 9 displays the information of the wavelength, oscillator strength and contribution of the MOs to the corresponding electronic transitions. In the case of model **3**, there are five electronic transitions of large oscillator strength value between 360 and 424 nm. The computed wavelength values agree well with the corresponding excitation spectrum obtained for this complex that shows a maximum at 330 nm with a tail extending up to ca. 430 nm. The main contributions to these five electronic transitions involve the above commented molecular orbitals, which seems to indicate that the origin of the luminescent properties in **3** would be related to metal-perturbed intra ligand transitions. In the case of **4,** similar behaviour was computed. The most intense electronic transitions appear around 296 nm, although less intense transitions appear around 310 nm. This result is also in agreement with the excitation spectrum registered for **4** between 275 and 350 nm, in which a maximum at 330 nm is obtained. Again, the analysis of the orbitals involved in the electronic transitions shows up a metal-perturbed intra ligand transitions as the origin of the emissive properties of this complex.

Table 9. TD-DFT singlet-singlet excitation calculations for model systems of **3** and **4**.

		3	
Transition	λ/nm	Oscillator strength	Contributions
S_0-S_1	424.1	0.0772	HOMO→LUMO+2 (95%)
S_0-S_2	316.0	0.0404	HOMO→LUMO (54%) HOMO-1→LUMO+1 (31%)
S_0-S_5	390.9	0.0111	HOMO→LUMO (35%) HOMO-4→LUMO (30%) HOMO-1→LUMO+1 (16%)
S_0-S_7	368.4	0.0233	HOMO-5→LUMO (40%) HOMO-6→LUMO+1 (25%)
S_0-S_{10}	360.3	0.0152	HOMO-5→LUMO+2 (50%) HOMO-4→LUMO+2 (41%)
		4	
S_0-S_4	298.9	0.0155	HOMO→LUMO+3 (46%) HOMO-1→LUMO+2 (38%)
S_0-S_7	296.4	0.133	HOMO-8→LUMO (40%) HOMO-7→LUMO+1 (18%) HOMO-9→LUMO+1 (18%)
S_0-S_8	295.7	0.124	HOMO-2→LUMO+3 (46%) HOMO-3→LUMO+2 (37%)

4. CONCLUSION

Four new Ag(I) coordination polymers with L and aromatic polyoxoacids as co-ligands were synthesized and characterized. Compounds **1** and **2** crystallize in the tetragonal $P\text{–}42_1m$ and triclinic $P\text{–}1$ space group, respectively, while **3** and **4** crystallize in the same monoclinic $P2_1/n$ space group. L behaves as a *bis*-monodentate ligand in all four structures, while the Ag(I) ion is three-coordinated in **2**, and four-coordinated in all the other complexes. Thermal analysis showed that all four complexes have good thermal stability, with the onset of the thermal decomposition in 170–240 °C temperature range. Investigation of intermolecular interactions evinced that **2** and **4** exhibit considerable contribution of interactions with the metal center, while the almost

complete absence of such interactions in **3** can be attributed to the tetrahedral coordination of Ag. While all compounds have similar values of the intermolecular interaction energies, the origin of those interactions is different and can be correlated with the type of co-ligand in the structure. Photocatalytic properties were measured for photocatalytic degradation of MB9 dye, and show that all four complexes exhibit reasonable reaction rates. The differences are attributed to the different co-ligands, where both the type and coordination of the co-ligand can be correlated with changes in the photocatalytic reaction rate. When irradiated with the UV light, **3** and **4** show photoluminescent emission, with **4** exhibiting luminescence at both RT and 77 K. The luminescence lifetimes for **3** and **4** suggest electronic transitions of singlet parentage. Since the excitation spectra appear to overlap with the wavelength range of the corresponding absorption spectra in the solid state, these transitions are most likely allowed and related to fluorescence processes. TD-DFT study determined the relative contributions of individual singlet-singlet electronic excitations to the fluorescence properties of both complexes, indicating that metal-perturbed intra ligand transitions is responsible in both cases.

ASSOCIATED CONTENT

Supporting information available

Supplementary information contains crystallographic data and refinement parameters for SQUEEZED structure **3**, pairwise interaction energies in the crystal structure of **1–4** based on B3LYP/ DGDZVP energy model, overlapped experimental and theoretically obtained powder X-ray diffractograms and photocatalytic degradation of MB9 dye using the complexes **1–4** monitored by UV-Vis spectroscopy. This information is available free of charge via the Internet at http://pubs.acs.org/.

Accession Codes

CCDC 1987944, 1987947–1987949 and 1990303 contain the supplementary crystallographic data for this paper. These data can be obtained free of charge via www.ccdc.cam.ac.uk/data_request/cif or by emailing data_request@ccdc.cam.ac.uk, or by contacting The Cambridge Crystallographic Data Centre, 12 Union Road, Cambridge CB2 1EZ, UK; fax: +44 1223 336033.

AUTHOR INFORMATION

Corresponding author

*E-mail: tamarat@chem.bg.ac.rs. Telephone: +381 11 3336731

ORCID

Predrag Ristić: 0000-0002-7489-6132

Tamara R. Todorović: 0000-0002-7740-3639

Vladimir Blagojević: 0000-0001-8102-989X

Olivera R. Klisurić: 0000-0003-0524-8139

Ivana Marjanović 0000-0003-4078-2556

Berta Barta Holló: 0000-0002-5786-442X

Predrag Vulić: 0000-0002-4806-4551

Mihaela Gulea: 0000-0002-2945-0078

Morgan Donnard: 0000-0002-9303-4634

María Rodríguez-Castillo: 0000-0002-9450-2305

Miguel Monge: 0000-0002-9672-8279

José M. López-de-Luzuriaga: 0000-0001-5767-8734

Nenad R. Filipović: 0000-0003-2982-5324

Notes

The authors declare no competing financial interest.

ACKNOWLEDGMENTS

The authors gratefully acknowledge financial support from the Ministry of Education, Science and Technological Development of Republic of Serbia, contract numbers 451-03-68/2020-14/200116 and 451-03-68/2020-14/200168. The D.G.I.(MEC)/FEDER (CTQ2016-75816-C02-02-P) project is acknowledged for financial support. BBH and NRF gratefully acknowledge help from prof. Katalin Mészáros Szécsényi, University of Novi Sad, Faculty of Sciences for her support and valuable advices in TG analysis.

REFERENCES

(1) Shen, C.; Xu, Y.; Lu, M. A Series of High-Energy Coordination Polymers with 3,6-Bis(4-Nitroamino-1,2,5-Oxadiazol-3-Yl)-1,4,2,5-Dioxadiazine, a Ligand with Multi-Coordination Sites, High Oxygen Content and Detonation Performance: Syntheses, Structures, and Performance. *J. Mater. Chem. A* **2017**, *5*, 18854–18861.

(2) Wu, X. Y.; Qi, H. X.; Ning, J. J.; Wang, J. F.; Ren, Z. G.; Lang, J. P. One Silver(I)/Tetraphosphine Coordination Polymer Showing Good Catalytic Performance in the Photodegradation of Nitroaromatics in Aqueous Solution. *Appl. Catal. B Environ.* **2015**, *168–169*, 98–104.

(3) San Sebastian, E.; Rodríguez-Diéguez, A.; Seco, J. M.; Cepeda, J. Coordination Polymers with Intriguing Photoluminescence Behavior: The Promising Avenue for Greatest Long-Lasting Phosphors. *Eur. J. Inorg. Chem.* **2018**, *2018*, 2155–2174.

(4) Mirtamizdoust, B. Sonochemical Synthesis of Nano Lead(II) Metal-Organic Coordination Polymer; New Precursor for the Preparation of Nano-Materials. *Ultrason. Sonochem.* **2017**, *35*, 263–269.

(5) Molaei, F.; Bigdeli, F.; Morsali, A.; Joo, S. W.; Bruno, G.; Rudbari, H. A. Synthesis and Characterization of Different Zinc(II) Oxide Nano-Structures from Two New Zinc(II)-Quinoxaline Coordination Polymers. *J. Mol. Struct.* **2015**, *1095*, 8–14.

(6) Xing, B.; Choi, M. F.; Xu, B. Design of Coordination Polymer Gels as Stable Catalytic Systems. *Chem. - Eur. J.* **2002**, *8*, 5028–5032.

(7) Kim, T. H.; Shin, Y. W.; Lee, S. S.; Kim, J. Supramolecular Assembly of One-Dimensional Channels and Two-Dimensional Brick-Wall Networks from Asymmetric Dithioether Ligands and Copper(I) Iodide. *Inorg. Chem. Commun.* **2007**, *10*, 11–14.

(8) Maurya, M. R.; Kumar, A. Oxovanadium(IV) Based Coordination Polymers and Their Catalytic Potentials for the Oxidation of Styrene, Cyclohexene and Trans-Stilbene. *J. Mol. Catal. A Chem.* **2006**, *250*, 190–198.

(9) Blagojević, V. A.; Lukić, V.; Begović, N. N.; Maričić, A. M.; Minić, D. M. Hydrogen

Storage in a Layered Flexible $[Ni_2(Btc)(En)_2]n$ Coordination Polymer. *Int. J. Hydrogen Energy* **2016**, *41*, 22171–22181.

(10) Hasegawa, Y.; Kitagawa, Y. Thermo-Sensitive Luminescence of Lanthanide Complexes, Clusters, Coordination Polymers and Metal-Organic Frameworks with Organic Photosensitizers. *J. Mater. Chem. C* **2019**, *7*, 7494–7511.

(11) Wang, H. N.; Meng, X.; Dong, L. Z.; Chen, Y.; Li, S. L.; Lan, Y. Q. Coordination Polymer-Based Conductive Materials: Ionic Conductivity: Vs. Electronic Conductivity. *J. Mater. Chem. A* **2019**, *7*, 24059–24091.

(12) Mas-Ballesté, R.; Gómez-Herrero, J.; Zamora, F. One-Dimensional Coordination Polymers on Surfaces: Towards Single Molecule Devices. *Chem. Soc. Rev.* **2010**, *39*, 4220–4233.

(13) McDonald, K. A.; Seth, S.; Matzger, A. J. Coordination Polymers with High Energy Density: An Emerging Class of Explosives. *Cryst. Growth Des.* **2015**, *15*, 5963–5972.

(14) Zhou, B.; Yan, D. Simultaneous Long-Persistent Blue Luminescence and High Quantum Yield within 2D Organic–Metal Halide Perovskite Micro/Nanosheets. *Angew. Chem., Int. Ed.* **2019**, *58*, 15128–15135.

(15) Yang, X.; Yan, D. Direct White-Light-Emitting and near-Infrared Phosphorescence of Zeolitic Imidazolate Framework-8. *Chem. Commun.* **2017**, *53*, 1801–1804.

(16) Morsali, A.; Hashemi, L. *Main Group Metal Coordination Polymers: Stuctures and Nanostructures,* John Wiley & Sons, Inc.: Hoboken, New Jersey, 2017.

(17) Tran, M.; Kline, K.; Qin, Y.; Shen, Y.; Green, M. D.; Tongay, S. 2D Coordination Polymers: Design Guidelines and Materials Perspective. *Appl. Phys. Rev.* **2019**, *6,* 041311–041328.

(18) Allen, F. H. The Cambridge Structural Database: A Quarter of a Million Crystal Structures and Rising. *Acta Crystallogr. Sect. B* **2002**, *58*, 380–388.

(19) Zhu, H.; Liu, D.; Li, Y. H.; Cui, G. H. A 1D Silver(I) Coordination Polymer as

Luminescent Probe for Cu^{2+} and Effective Photocatalyst for Degradation Organic Dyes. *Inorg. Chem. Commun.* **2019**, *108*, 107539.

(20) Dinh Do, N.; Kovalchukova, O.; Stash, A.; Strashnova, S. Catena-Poly[Ammonium [Aquabis(μ-2,3,5,6-Tetraoxo-4-Nitropyridin-4-Ido) Argentate(I)]]. *Acta Crystallogr. Sect. E Struct. Reports Online* **2013**, *69*, 477–478.

(21) Fang, X. Q.; Deng, Z. P.; Huo, L. H.; Wan, W.; Zhu, Z. B.; Zhao, H.; Gao, S. New Family of Silver(I) Complexes Based on Hydroxyl and Carboxyl Groups Decorated Arenesulfonic Acid: Syntheses, Structures, and Luminescent Properties. *Inorg. Chem.* **2011**, *50*, 12562–12574.

(22) Chen, C. L.; Kang, B. S.; Su, C. Y. Recent Advances in Supramolecular Design and Assembly of Silver(I) Coordination Polymers. *Aust. J. Chem.* **2006**, *59*, 3–18.

(23) Capel Berdiell, I.; Warriner, S. L.; Halcrow, M. A. Silver(I) Complexes of Bis- and Tris-(Pyrazolyl)Azine Derivatives-Dimers, Coordination Polymers and a Pentametallic Assembly. *Dalton Trans.* **2018**, *47*, 5269–5278.

(24) Khlobystov, A. N.; Blake, A. J.; Champness, N. R.; Lemenovskii, D. A.; Majouga, A. G.; Zyk, N. V.; Schröder, M. Supramolecular Design of One-Dimensional Coordination Polymers Based on Silver(I) Complexes of Aromatic Nitrogen-Donor Ligands. *Coord. Chem. Rev.* **2001**, *222*, 155–192.

(25) Paper, R. All Procedures for the Synthesis of Silver Nanosheets. *Nanochem. Res.* **2017**, *2*, 248–260.

(26) Huang, Z.; Du, M.; Song, H. Bin; Bu, X. H. Effect of Anions on the Framework Formation of Novel AgI Coordination Polymers with Angular Bridging Ligands. *Cryst. Growth Des.* **2004**, *4*, 71–78.

(27) Zorlu, Y.; Can, H.; Aksakal, F. A Novel 2D Chiral Silver(I) Coordination Polymer Assembled from 5-Sulfosalicylic Acid and (2S,4R)-4-Hydroxyproline: Synthesis, Crystal Structure, HOMO-LUMO and NBO Analysis. *J. Mol. Struct.* **2013**, *1049*, 368–376.

(28) Gupta, A. K.; Salazar, D. M.; Orthaber, A. Solvent and Counter-Ion Induced Coordination

Environment Changes Towards AgI Coordination Polymers. *Eur. J. Inorg. Chem.* **2019**, *33*, 3740–3744.

(29) Kim, H. J.; Zin, W. C.; Lee, M. Anion-Directed Self-Assembly of Coordination Polymer into Tunable Secondary Structure. *J. Am. Chem. Soc.* **2004**, *126*, 7009–7014.

(30) Roy, S.; Titi, H. M.; Tripuramallu, B. K.; Bhunia, N.; Verma, R.; Goldberg, I. Silver Coordination Polymers Based on Newly Designed Bis(Cyanobenzyl)Bipiperidine Ligand: Synthesis, Anion Exchange, Guest Inclusion, Electrochemical, and Photoluminescence Properties. *Cryst. Growth Des.* **2016**, *16*, 2814–2825.

(31) Xie, Y. P.; Al-Thabaiti, S. A.; Mokhtar, M.; Mak, T. C. W. An Unusual Silver-Ethynide Polymeric Chain Containing Centrosymmetric Ag14 Cluster Segments Stabilized by Mixed Carboxylate Ligands. *Inorg. Chem. Commun.* **2013**, *31*, 54–57.

(32) Moon, S. H.; Kang, Y.; Park, K. M. Crystal Structure of a Twisted-Ribbon Type Double-Stranded Ag^{I} Coordination Polymer: Catena-poly-[[silver(I)-μ_3-bis(pyridin-3-ylmethyl)sulfane-k^{3}N:N':S] nitrate]. *Acta Crystallogr. Sect. E Crystallogr. Commun.* **2017**, *73*, 1587–1589.

(33) Rath, B. B.; Kole, G. K.; Vittal, J. J. Structural Transformation of Photoreactive Helical Coordination Polymers to Two-Dimensional Structures. *Cryst. Growth Des.* **2018**, *18*, 6221–6226.

(34) Cheng, L.; Zhang, L.; Cao, Q.; Gou, S.; Zhang, X.; Fang, L. Temperature-Induced Chiral Ag(I) Coordination Polymers with Structural Variation from 1D to 2D: Synthesis, Luminescence and SHG Response. *CrystEngComm* **2012**, *14*, 7502–7510.

(35) Kole, G. K.; Vittal, J. J. Solid-State Reactivity and Structural Transformations Involving Coordination Polymers. *Chem. Soc. Rev.* **2013**, *42*, 1755–1775.

(36) Li, C. P.; Zhou, H.; Wang, S.; Chen, J.; Wang, Z. L.; Du, M. Highly Efficient $Cr_2O_7^{2-}$ Removal of a 3D Metal-Organic Framework Fabricated by Tandem Single-Crystal to Single-Crystal Transformations from a 1D Coordination Array. *Chem. Commun.* **2017**, *53*, 9206–9209.

(37) Arii, H.; Saito, Y.; Funahashi, Y.; Ozawa, T.; Jitsukawa, K.; Masuda, H. Silver(I) Complex Crystals Switched by a Water Molecule. *Eur. J. Inorg. Chem.* **2003**, 16, 2917–2919.

(38) Fukushima, M.; Kikkawa, S.; Hikawa, H.; Azumaya, I. Synthesis and Solvent Vapor-Induced Transformations of Crystals of 1D Coordination Polymers Assembled with Continuous Void Space. *CrystEngComm* **2017**, *19*, 3398–3406.

(39) Kim, D.; Park, S.; Jung, O. S. In Situ Two-Step Crystallization: Transformation of Kinetic Crystals into Thermodynamic Crystals. *Cryst. Growth Des.* **2019**, *19*, 2019–2023.

(40) Yang, X.; Wang, Y.; Zhou, H. L.; Liu, Y. J.; He, C. T.; Lin, R. B.; Zhang, J. P. Guest-Containing Supramolecular Isomers of Silver(I) 3,5-Dialkyl-1,2,4-Triazolates: Syntheses, Structures, and Structural Transformation Behaviours. *CrystEngComm* **2015**, *17*, 8843–8849.

(41) Sushrutha, S. R.; Mohana, S.; Pal, S.; Natarajan, S. Solvent-Dependent Delamination, Restacking, and Ferroelectric Behavior in a New Charge-Separated Layered Compound: $[NH_4][Ag_3(C_9H_5NO_4S)_2(C_{13}H_{14}N_2)_2]\cdot 8\,H_2O$. *Chem. - Asian J.* **2017**, *12*, 101–109.

(42) Azizzadeh, S.; Nobakht, V.; Carlucci, L.; Proserpio, D. M. Anion-Directed Assembly of Three Cationic Silver(I) Coordination Polymers with Bis(Imidazolyl)-Based Linker: Structural Characterization and Anion Exchange Study. *Polyhedron* **2020**, *175*, 114236.

(43) Adarsh, N. N.; Novio, F.; Ruiz-Molina, D. Coordination Polymers Built from 1,4-Bis(Imidazol-1-Ylmethyl)Benzene: From Crystalline to Amorphous. *Dalton Trans.* **2016**, *45*, 11233–11255.

(44) Trivedi, M.; Singh, G.; Kumar, A.; Rath, N. P. Silver(I) Complexes as Efficient Source for Silver Oxide Nanoparticles with Catalytic Activity in A3 Coupling Reactions. *Inorg. Chim. Acta* **2015**, *438*, 255–263.

(45) Zisti, F.; Tehrani, A. A.; Alizadeh, R.; Abbasi, H.; Morsali, A.; Eichhorn, S. H. Synthesis and Structural Characterization of Three Nano-Structured Ag(I) Coordination Polymers; Syntheses, Characterization and X-Ray Crystal Structural Analysis. *J. Solid State Chem.*

2019, *271*, 29–39.

(46) Tatikonda, R.; Bulatov, E.; Özdemir, Z.; Nonappa; Haukka, M. Infinite coordination polymer networks: metallogelation of aminopyridine conjugates and *in situ* silver nanoparticle formation. *Soft Matter* **2019**, *15*, 442–451.

(47) Cheng, Y.; Yin, M.; Ren, X.; Feng, Q.; Wang, J.; Zhou, Y. A Coordination Polymeric Gelator Based on Ag(I) and 2, 7-Bis(1-Imidazole)Fluorene: Synthesis, Characterization, Gelation and Antibacterial Properties. *Mater. Lett.* **2015**, *139*, 141–144.

(48) Paquin, F.; Rivnay, J.; Salleo, A.; Stingelin, N.; Silva, C. Multi-Phase Semicrystalline Microstructures Drive Exciton Dissociation in Neat Plastic Semiconductors. *J. Mater. Chem. C* **2015**, *3*, 10715–10722.

(49) Biswas, P.; Ganguly, S.; Dastidar, P. Stimuli-Responsive Metallogels for Synthesizing Ag Nanoparticles and Sensing Hazardous Gases. *Chem. - Asian J.* **2018**, *13*, 1941–1949.

(50) Paul, M.; Sarkar, K.; Dastidar, P. Metallogels Derived from Silver Coordination Polymers of C3-Symmetric Tris(Pyridylamide) Tripodal Ligands: Synthesis of Ag Nanoparticles and Catalysis. *Chem. - Eur. J.* **2015**, *21*, 255–268.

(51) Tan, X.; Chen, X.; Zhang, J.; Su, C. Y. Luminescent Coordination Polymer Gels Based on Rigid Terpyridyl Phosphine and Ag(I). *Dalton Trans.* **2012**, *41*, 3616–3619.

(52) Wu, L.; Han, C.; Wu, X.; Wang, L.; Caochen, Y.; Jing, X. Reversible Formation of Supramolecular Polymer Networks via Orthogonal Pillar[10]Arene-Based Host-Guest Interactions and Metal Ion Coordinations. *Dalton Trans.* **2015**, *44*, 20334–20337.

(53) Rogovoy, M. I.; Berezin, A. S.; Kozlova, Y. N.; Samsonenko, D. G.; Artem'ev, A. V. A Layered Ag(I)-Based Coordination Polymer Showing Sky-Blue Luminescence and Antibacterial Activity. *Inorg. Chem. Commun.* **2019**, *108*, 107513.

(54) Wang, G.; Chen, T.; Wang, X.; Ma, H.; Pang, H. High-Performance Supercapacitor Afforded by a High-Connected Keggin-Based 3D Coordination Polymer. *Eur. J. Inorg. Chem.* **2017**, *2017*, 5350–5355.

(55) Du, J.; Sun, X.; He, Y.; Yu, Y.; Zheng, X.; Tian, L.; Liu, Z. The Proton Conductivities of Two Silver-Thiophene-2-Carboxylate Coordination Polymer and the Relationship between the Dimensionality and Properity. *Appl. Organomet. Chem.* **2018**, *32*, e4517.

(56) Cheng, Q. X.; Lan, J. J.; Chen, Y. Q.; Lin, J.; Chenna Krishna Reddy, R.; Lin, X. M.; Cai, Y. P. 1D Helical Silver(I)-Based Coordination Polymer Containing Pyridyl Diimide Ligand for Fe(III) Ions Detection. *Inorg. Chem. Commun.* **2018**, *96*, 30–33.

(57) Soe, E.; Ehlke, B.; Oliver, S. R. J. A Cationic Silver Pyrazine Coordination Polymer with High Capacity Anion Uptake from Water. *Environ. Sci. Technol.* **2019**, *53*, 7663–7672.

(58) Baraka, A.; Hatem, H.; El-Geundi, M. S.; Tantawy, H.; Karaghiosoff, K.; Gobara, M.; Elbeih, A.; Shoaib, M.; Elsayed, M. A.; Kotb, M. M. A New Cationic Silver(I)/Melamine Coordination Polymer, $[Ag_2(Melamine)]_n^{2n+}$: Synthesis, Characterization and Potential Use for Aqueous Contaminant Anion Exchange. *J. Solid State Chem.* **2019**, *274*, 168–175.

(59) Zhao, X. X.; Liu, D.; Li, Y. H.; Cui, G. H. Bifunctional Silver(I) Coordination Polymer Exhibiting Selective Adsorptive of Congo Red and Luminescent Sensing for Ferric Ion. *Polyhedron* **2018**, *156*, 80–88.

(60) Li, C. P.; Zhou, H.; Wang, J. J.; Liu, B. L.; Wang, S.; Yang, X.; Wang, Z. L.; Liu, C. Sen; Du, M.; Zhou, W. Mechanism-Property Correlation in Coordination Polymer Crystals toward Design of a Superior Sorbent. *ACS Appl. Mater. Interfaces* **2019**, *11*, 42375–42384.

(61) Ye, C. P.; Xu, G.; Wang, Z.; Han, J.; Xue, L.; Cao, F. Y.; Zhang, Q.; Yang, L. F.; Lin, L. Z.; Chen, X. D. Design and Synthesis of Functionalized Coordination Polymers as Recyclable Heterogeneous Photocatalysts. *Dalton Trans.* **2018**, *47*, 6470–6478.

(62) Liu, C. F.; Liu, C. Y.; Ren, Z. G.; Lang, J. P. Silver(I)-Based Complexes Used as High-Performance Photocatalysts for the Degradation of Organic Dyes in Water. *Eur. J. Inorg. Chem.* **2019**, *2019*, 1816–1824.

(63) Mandal, S.; Nanavati, S. P.; Willock, D. J.; Ananthakrishnan, R. Photoactive Ag(I)-Based Coordination Polymer as a Potential Semiconductor for Photocatalytic Water Splitting and

Environmental Remediation: Experimental and Theoretical Approach. *J. Phys. Chem. C* **2019**, *123*, 23940–23950.

(64) Kumar, G.; Pandey, S.; Gupta, R. Ag-Based Coordination Polymers Based on Metalloligands and Their Catalytic Performance in Multicomponent A 3 -Coupling Reactions. *Cryst. Growth Des.* **2018**, *18*, 5501–5511.

(65) Liu, J. Q.; Luo, Z. D.; Pan, Y.; Kumar Singh, A.; Trivedi, M.; Kumar, A. Recent Developments in Luminescent Coordination Polymers: Designing Strategies, Sensing Application and Theoretical Evidences. *Coord. Chem. Rev.* **2020**, *406*, 213145.

(66) Yang, X.; Lin, X.; Zhao, Y.; Zhao, Y. S.; Yan, D. Lanthanide Metal–Organic Framework Microrods: Colored Optical Waveguides and Chiral Polarized Emission. *Angew. Chem., Int. Ed.* **2017**, *56*, 7853–7857.

(67) Yang, Y.; Wang K.; Yan D. Smart Luminescent Coordination Polymers toward Multimode Logic Gates: Time-Resolved, Tribochromic and Excitation-Dependent Fluorescence/Phosphorescence Emission. *ACS Appl. Mater. Interfaces* **2017,** *9*, 17399–17407.

(68) Yang, Y.; Wang K.; Yan D. Ultralong Persistent Room Temperature Phosphorescence of Metal Coordination Polymers Exhibiting Reversible pH-Responsive Emission. *ACS Appl. Mater. Interfaces* **2016**, *8*, 15489–15496.

(69) Lu, S. H.; Li, Y.; Yang, S. X.; Zhao, R. D.; Lu, Z. X.; Liu, X. L.; Qin, Y.; Zheng, L. Y.; Cao, Q. E. Three Silver Coordination Polymers with Diverse Architectures Constructed from Pyridine Carboxylic Hydrazide Ligands. *Inorg. Chem.* **2019**, *58*, 11793–11800.

(70) Lewis, J. E. M. Self-Templated Synthesis of Amide Catenanes and Formation of a Catenane Coordination Polymer. *Org. Biomol. Chem.* **2019**, *17*, 2442–2447.

(71) Liang, N.; Cui, Y. F.; Yuan, D. Y.; Li, B. L.; Li, H. Y. Anion-Controlled Four Silver Coordination Polymers with Flexible Bis(1,2,4-Triazol-4-Yl)Ethane. *Inorg. Chim. Acta* **2011**, *376*, 612–618.

(72) Dennehy, M.; Delgado, F.; Freire, E.; Halac, E.; Baggio, R. A Polymeric Silver

Thiosaccarinate Complex with a Two-Dimensional Triply Entangled Mesh and Argentophilic Interactions. *Acta Crystallogr. Sect. C Struct. Chem.* **2016**, *72*, 572–577.

(73) Ma, J. F.; Yang, J.; Li, S. L.; Song, S. Y.; Zhang, H. J.; Wang, H. S.; Yang, K. Y. Two Coordination Polymers of Ag(I) with 5-Sulfosalicylic Acid. *Cryst. Growth Des.* **2005**, *5*, 807–812.

(74) Huang, H. Q.; Wang, D. F.; Zhang, T.; Huang, R. Bin. Effects of Different Carboxylates on Ag(I) Coordination Compounds with Pyrazinamide and Pyrazinecarbonitrile with in Situ Reaction Ligands. *J. Mol. Struct.* **2015**, *1086*, 99–108.

(75) Al-Nubi, M. A. A.; Hamisu, A. M.; Wardana, F. Y.; Ariffin, A.; Jo, H.; Ok, K. M.; Wibowo, A. C. Lead-Organic Frameworks Containing Trimesic Acid: Facile Dissolution-Crystallization and Near-White Light Emission. *Cryst. Growth Des.* **2019**, *19*, 6274–6282.

(76) Arici, M.; Yeşilel, O. Z.; Yeşilöz, Y.; Şahin, O. One- and Three-Dimensional Silver(I)-5-Sulfosalicylate Coordination Polymers Having Ligand-Supported and Unsupported Argentophilic Interactions. *J. Solid State Chem.* **2014**, *220*, 70–78.

(77) Luo, G. G.; Sun, D.; Xu, Q. J.; Zhang, N.; Huang, R. Bin; Lin, L. R.; Zheng, L. S. Photoluminescent Metal-Organic Coordination Polymer Incorporating One-Dimensional Silver Chains. *Inorg. Chem. Commun.* **2009**, *12*, 436–439.

(78) Sun, D.; Cao, R.; Weng, J.; Hong, M.; Liang, Y. A Novel Luminescent 3D Polymer Containing Silver Chains Formed by Ligand Unsupported Ag-Ag Interactions and Organic Spacers. *J. Chem. Soc., Dalton Trans.* **2002**, *1*, 291–292.

(79) Sun, D.; Zhang, N.; Luo, G. G.; Xu, Q. J.; Huang, R. Bin; Zheng, L. S. Assembly of Silver(I) Coordination Polymers Incorporating Pyromellitic Acid and N-Heterocyclic Ligands. *Polyhedron* **2010**, *29*, 1842–1848.

(80) Zhang, J.; Wang, C. C.; Wang, P.; Guo, X. X.; Gao, S. J. Silver-Based Coordination Complexes of Carboxylate Ligands: Crystal Structures, Luminescence and Photocatalytic Properties. *Transition Met. Chem.* **2016**, *41*, 637–645.

(81) Cheng, X. Y.; Miao, R. Q.; Zhong, Y. Y.; Huang, R. Bin; Zheng, L. S. Syntheses,

Structures, and Properties of Four Novel Ag(I) Coordination Polymers Based on 2,6-Dimethylpyrazine and Benzene Dicarboxylates. *Inorg. Chem. Commun.* **2017**, *86*, 192–199.

(82) Shi, X.; Tan, D.; Liu, Y.; Liang, G.; Zhang, X. Syntheses, Structures and Fluorescence Properties of Two Novel Polymers Based on a Flexible Tripodal Ligand 1,3,5-Tris((1H-1,2,4-Triazol-1-Yl)Methyl) Benzene. *J. Mol. Struct.* **2014**, *1074*, 134–139.

(83) Miao, S. Bin; Li, Z. H.; Xu, C. Y.; Ji, B. M. Syntheses, Characterization, and Luminescence Properties of Three Novel Ag(I) Coordination Polymers Based on Polycarboxylic Acid Ligands and 1,3-di-(1,2,4-triazole-4-yl)benzene. *CrystEngComm* **2016**, *18*, 4636–4642.

(84) Wang, D.; Wang, Z.; Zhang, T.; Dai, S.; Huang, R.-B.; Zheng, L.-S. Syntheses, Characterizations, Thermal Stability and Photoluminescence of Four Silver Coordination Polymers with Mixed Ligands. *Inorg. Chim. Acta* **2014**, *415*, 61–68.

(85) Kan, W. Q.; Wen, S. Z.; Kan, Y. H.; Hu, H. Y.; Niu, S. Y.; Zhang, X. Y. Syntheses, Structures, Characterization and Photoluminescent Properties of Six Coordination Polymers Based on Multidentate N-Donor Ligands and Polycarboxylate Anions. *Polyhedron* **2015**, *85*, 246–254.

(86) Wang, D. F.; Wang, Z. H.; Zhang, T.; Dai, S. M.; Huang, R. Bin; Zheng, L. S. Syntheses, Characterizations, Thermal Stability and Photoluminescence of Four Silver Coordination Polymers with Mixed Ligands. *Inorg. Chim. Acta* **2014**, *415*, 61–68.

(87) Teng, F.; Yu, J. T.; Jiang, Y.; Yang, H.; Cheng, J. A Copper-Mediated Oxidative N-Cyanation Reaction. *Chem. Commun.* **2014**, *50*, 8412–8415.

(88) Rigaku OD (2015). CrysAlis PRO. Rigaku Oxford Diffraction Ltd, Yarnton, Oxfordshire, England. 2015.

(89) Bruker (2010). APEX3, SAINT and SADABS. Bruker AXS Inc., Madison, Wisconsin, USA. 2010.

(90) Clark, R. C.; Reid, J. S. The Analytical Calculation of Absorption in Multifaceted

Crystals. *Acta Crystallogr. Sect. A* **1995**, *51*, 887–897.

(91) Sheldrick, G. M. *SHELXT* – Integrated Space-Group and Crystal-Structure Determination. *Acta Crystallogr. Sect. A Found. Adv.* **2015**, *71*, 3–8.

(92) Sheldrick, G. M. Crystal Structure Refinement with SHELXL. *Acta Crystallogr. Sect. C Struct. Chem.* **2015**, C*71*, 3–8.

(93) Bruno, I. J.; Cole, J. C.; Edgington, P. R.; Kessler, M.; Macrae, C. F.; McCabe, P.; Pearson, J.; Taylor, R. New Software for Searching the Cambridge Structural Database and Visualizing Crystal Structures. *Acta Crystallogr. Sect. B Struct. Sci.* **2002**, *58*, 389–397.

(94) Farrugia, L. J. WinGX Suite for Small-Molecule Single-Crystal Crystallography. *J. Appl. Crystallogr.* **1999**, *32*, 837–838.

(95) Spek, A. L. Structure Validation in Chemical Crystallography. *Acta Crystallogr. Sect. D Biol. Crystallogr.* **2009**, *65*, 148–155.

(96) Blatov, V. A.; Shevchenko, A. P.; Proserpio, D. M. Applied Topological Analysis of Crystal Structures with the Program Package Topospro. *Cryst. Growth Des.* **2014**, *14*, 3576–3586.

(97) McKinnon, J. J.; Jayatilaka, D.; Spackman, M. A. Towards Quantitative Analysis of Intermolecular Interactions with Hirshfeld Surfaces. *Chem. Commun.* **2007**, 37, 3814–3816.

(98) McKinnon, J. J.; Spackman, M. A.; Mitchell, A. S. Novel Tools for Visualizing and Exploring Intermolecular Interactions in Molecular Crystals; *Acta Crystallogr. Sect. B Struct. Sci.* **2004**, 60, 627**–**668.

(99) Frisch, M. J.; Trucks, G. W.; Schlegel, H. B.; Scuseria, G. E.; Robb, M. A.; Cheeseman, J. R.; Scalmani, G.; Barone, V.; Petersson, G. A.; Nakatsuji, H.; Li, X.; Caricato, M.; Marenich, A.; Bloino, J.; Janesko, B. G.; Gomperts, R.; Mennucci, B.; Hratchian, H. P.; Ortiz, J. V.; Izmaylov, A. F.; Sonnenberg, J. L.; Williams-Young, D.; Ding, F.; Lipparini, F.; Egidi, F.; Goings, J.; Peng, B.; Petrone, A.; Henderson, T.; Ranasinghe, D.;

Zakrzewski, V. G.; Gao, J.; Rega, N.; Zheng, G.; Liang, W.; Hada, M.; Ehara, M.; Toyota, K.; Fukuda, R.; Hasegawa, J.; Ishida, M.; Nakajima, T.; Honda, Y.; Kitao, O.; Nakai, H.; Vreven, T.; Throssell, K.; Montgomery, J. A. Jr.; Peralta, J. E.; Ogliaro, F.; Bearpark, M.; Heyd, J. J.; Brothers, E.; Kudin, K. N.; Staroverov, V. N.; Keith, T.; Kobayashi, R.; Normand, J.; Raghavachari, K.; Rendell, A.; Burant, J. C.; Iyengar, S. S.; Tomasi, J.; Cossi, M.; Millam, J. M.; Klene, M.; Adamo, C.; Cammi, R.; Ochterski, J. W.; Martin, R. L.; Morokuma, K.; Farkas, O.; Foresman, J. B.; Fox, D. J. Gaussian 09, Revision A.02, Gaussian, Inc., Wallingford CT, 2009.

(100) Mackenzie, C. F.; Spackman, P. R.; Jayatilaka, D.; Spackman, M. A. CrystalExplorer Model Energies and Energy Frameworks: Extension to Metal Coordination Compounds, Organic Salts, Solvates and Open-Shell Systems. *IUCrJ* **2017**, *4*, 575–587.

(101) Kumar, K. V.; Porkodi, K.; Rocha, F. Langmuir-Hinshelwood Kinetics - A Theoretical Study. *Catal. Commun.* **2008**, *9*, 82–84.

(102) Becke, A. D. Densityâ functional Thermochemistry. I. The Effect of the Exchange only Gradient Correction. *J. Chem. Phys.* **1992**, *96*, 2155–2160.

(103) Becke, A. D. Density-functional Thermochemistry. III. The Role of Exact Exchange. *J. Chem. Phys.* **1993**, *98*, 5648–5652.

(104) Lee, C.; Yang, W.; Parr, R. G. Development of the Colle-Salvetti Correlation-Energy Formula into a Functional of the Electron Density. *Phys. Rev. B* **1988**, *37*, 785–789.

(105) Ahlrichs, R.; Bär, M.; Häser, M.; Horn, H.; Kölmel, C. Electronic Structure Calculations on Workstation Computers: The Program System Turbomole. *Chem. Phys. Lett.* **1989**, *162*, 165–169.

(106) Bauernschmitt, R.; Ahlrichs, R. Treatment of Electronic Excitations within the Adiabatic Approximation of Time Dependent Density Functional Theory. *Chem. Phys. Lett.* **1996**, *256*, 454–464.

(107) Bauernschmitt, R.; Ahlrichs, R. Stability Analysis for Solutions of the Closed Shell Kohn-Sham Equation. *J. Chem. Phys.* **1996**, *104*, 9047–9052.

(108) Bauernschmitt, R.; Häser, M.; Treutler, O.; Ahlrichs, R. Calculation of Excitation Energies within Time-Dependent Density Functional Theory Using Auxiliary Basis Set Expansions. *Chem. Phys. Lett.* **1997**, *264*, 573–578.

(109) Gross, E. K. U.; Kohn, W. Time-Dependent Density-Functional Theory. *Adv. Quantum Chem.* **1990**, *21*, 255–291.

(110) Olsen, L.; Jorgensen, P. Time-Dependent Response Theory with Applications to Self-Consistent Field and Multiconfigurational Self-Consistent Field Wave Functions. In: *Modern Electronic Structure Theory*, *vol. 2*; Yarkony, D. R., Ed.; World Scientific: River Edge, NJ, 1995; pp 857–990.

(111) Schäfer, A.; Huber, C.; Ahlrichs, R. Fully Optimized Contracted Gaussian Basis Sets of Triple Zeta Valence Quality for Atoms Li to Kr. *J. Chem. Phys.* **1994**, *100*, 5829–5835.

(112) Schäfer, A.; Horn, H.; Ahlrichs, R. Fully Optimized Contracted Gaussian Basis Sets for Atoms Li to Kr. *J. Chem. Phys.* **1992**, *97*, 2571–2577.

(113) Weigend, F.; Ahlrichs, R. Balanced Basis Sets of Split Valence, Triple Zeta Valence and Quadruple Zeta Valence Quality for H to Rn: Design and Assessment of Accuracy. *Phys. Chem. Chem. Phys.* **2005**, *7*, 3297–3305.

(114) Andrae, D.; Häußermann, U.; Dolg, M.; Stoll, H.; Preuß, H. Energy-Adjusted Ab Initio Pseudopotentials for the Second and Third Row Transition Elements. *Theor. Chim. Acta* **1990**, *77*, 123–141.

(115) Yang, L.; Powell, D. R.; Houser, R. P. Structural Variation in Copper(I) Complexes with Pyridylmethylamide Ligands: Structural Analysis with a New Four-Coordinate Geometry Index, τ_4. *Dalton Trans.* **2007**, *9*, 955–964.

(116) Allen, F. H. Research Papers The Cambridge Structural Database : A Quarter of a Million Crystal Structures and Rising Research Papers. *Acta Cryst.* **2002**, *B58*, 380–388.

(117) Alexandrov, E. V.; Blatov, V. A.; Kochetkov, A. V.; Proserpio, D. M. Underlying Nets in Three-Periodic Coordination Polymers: Topology, Taxonomy and Prediction from a Computer-Aided Analysis of the Cambridge Structural Database. *CrystEngComm* **2011**,

13, 3947–3958.

(118) Spackman, M. A.; McKinnon, J. J. Fingerprinting Intermolecular Interactions in Molecular Crystals. *CrystEngComm* **2002**, *4*, 378–392.

(119) Maity, T.; Mandal, H.; Bauzá, A.; Samanta, B. C.; Frontera, A.; Seth, S. K. Quantifying Conventional C-H···π(Aryl) and Unconventional C-H···π(Chelate) Interactions in Dinuclear Cu(II) Complexes: Experimental Observations, Hirshfeld Surface and Theoretical DFT Study. *New J. Chem.* **2018**, *42*, 10202–10213.

(120) Berry, D. J.; Steed, J. W. Pharmaceutical Cocrystals, Salts and Multicomponent Systems; Intermolecular Interactions and Property Based Design. *Adv. Drug Deliv. Rev.* **2017**, *117*, 3–24.

(121) Prasad, M. R. R.; Sudhakarbabu, K. Thermal Decomposition of Tetraethyl Ammonium Tetrafluoroborate: A Simultaneous TG-DTG-DSC-Quadrupole Mass Spectrometric Approach. *J. Therm. Anal. Calorim.* **2014**, *115*, 1901–1905.

(122) Migdał-Mikuli, A.; Górska, N.; Szostak, E. Phase Transition and Thermal Decomposition of $[Al(DMSO)_6]Cl_3$. *J. Therm. Anal. Calorim.* **2007**, *90*, 223–228.

(123) Nikolova, D.; Georgiev, M. Synthesis, Thermal Investigations and Kinetic Data of $Zn(BF_4)_2 \cdot 6H_2O$. *J. Therm. Anal. Calorim.* **2009**, *95*, 319–321.

(124) Connelly, N. G.; Geiger, W. E. Chemical Redox Agents for Organometallic Chemistry. *Chem. Rev.* **1996**, *96*, 877–910.

(125) Lam, S. M.; Sin, J. C.; Abdullah, A. Z.; Mohamed, A. R. Degradation of Wastewaters Containing Organic Dyes Photocatalysed by Zinc Oxide: A Review. *Desalin. Water Treat.* **2012**, *41*, 131–169.

(126) Li, J.-X.; Qin, Z.-B.; Li, Y.-H.; Cui, G.-H. Sonochemical Synthesis and Properties of Two New Nanostructured Silver(I) Coordination Polymers. *Ultrason. Sonochem.* **2018**, *48*, 127–135.

(127) Lu, X. X.; Luo, Y. H.; Lu, C.; Chen, X.; Zhang, H. Assembly of Three New POM-Based

Ag(I) Coordination Polymers with Antibacterial and Photocatalytic Properties. *J. Solid State Chem.* **2015**, *232*, 123–130.

(128) Geng, J. C.; Qin, L.; Du, X.; Xiao, S. L.; Cui, G. H. Synthesis, Crystal Structures, and Catalytic Properties of Silver(I) and Cobalt(II) Coordination Polymers Based on Flexible Bis(Benzimidazole) with Pyridine-2, 6-Dicarboxylate. *Zeitschrift fur Anorg. und Allg. Chemie* **2012**, *638*, 1233–1238.

(129) Yang, Y. Y.; Zhou, L. X.; Zheng, Y. Q.; Zhu, H. L.; Li, W. Y. Hydrothermal Synthesis, Photoluminescence and Photocatalytic Properties of Two Silver(I) Complexes. *J. Solid State Chem.* **2017**, *253*, 211–218.

For Table of Contents Use Only

1D and 2D silver-based coordination polymers with thiomorpholine-4-carbonitrile and aromatic polyoxoacids as co-ligands: structure, photocatalysis, photoluminescence and TD-DFT study

Predrag Ristić, Tamara R. Todorović*, Vladimir Blagojević, Olivera R. Klisurić, Ivana Marjanović, Berta Barta Holló, Predrag Vulić, Mihaela Gulea, Morgan Donnard, Miguel Monge, María Rodríguez-Castillo, José M. López-de-Luzuriaga, Nenad R. Filipović

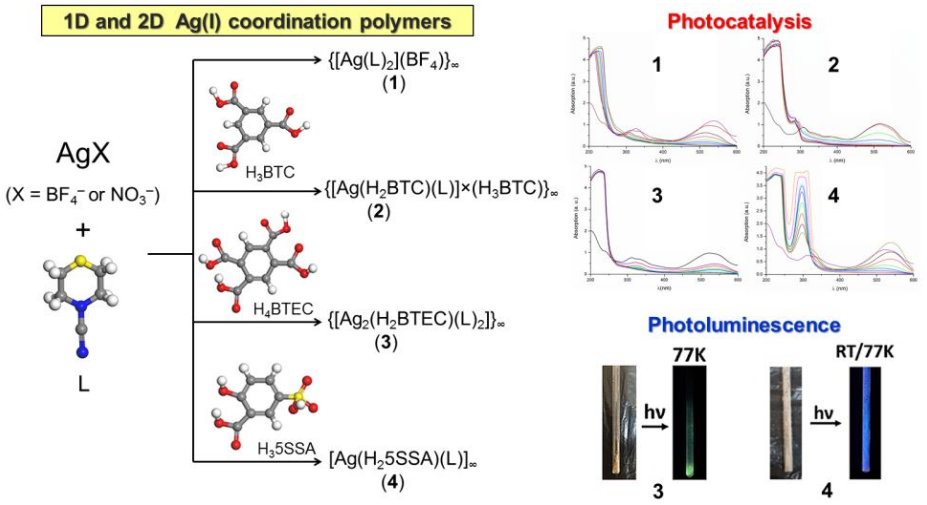

Ag(I) coordination polymers **1–4** exhibit reasonable reaction rates in photocatalytic degradation of MB9 dye. When irradiated with the UV light, **3** and **4** show photoluminescent emission. The luminescence lifetimes suggest electronic transitions of singlet parentage. TD-DFT study determined the relative contributions of individual singlet-singlet electronic excitations to the fluorescence properties, indicating that metal-perturbed intra ligand transitions is responsible in both cases.

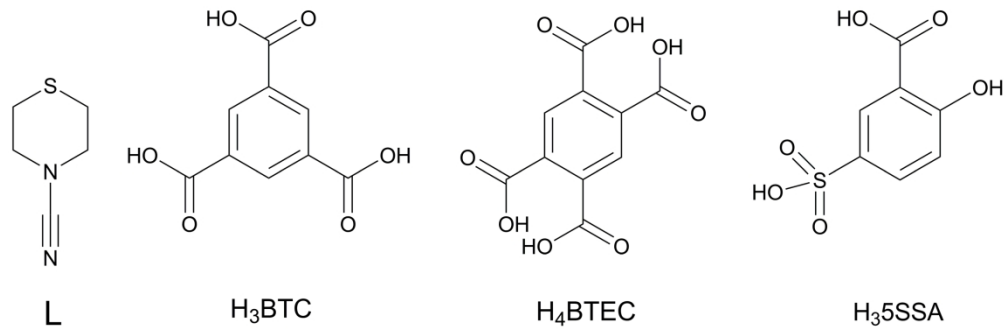

Figure 1. Structures of L and aromatic polyoxoacids co-ligands.

152x50mm (600 x 600 DPI)

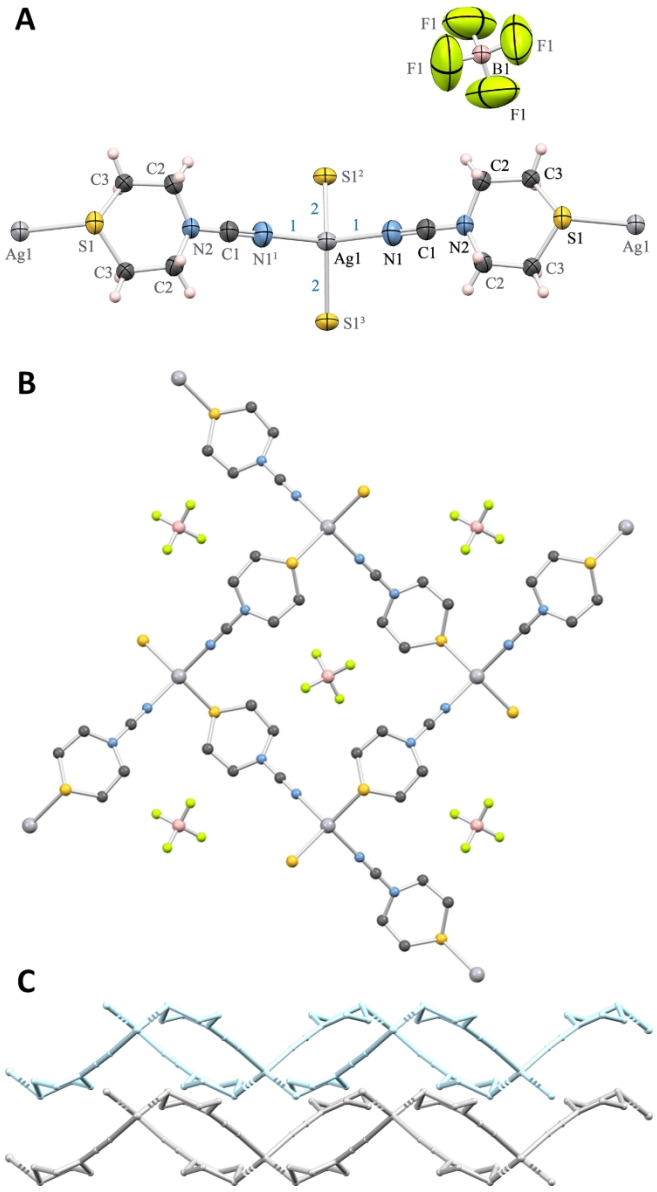

Figure 2. (A) ORTEP drawing (generated by MERCURY93) of the part of infinite structure of 1 with labeled non-H atoms. The atoms of the asymmetric unit are labeled in black. Displacement ellipsoids are shown at the 50% probability level, while the H atoms are drawn as spheres of arbitrary radii. Symmetry codes: (1) −x+1, −y, z; (2) y, −x+1, −z; (3) −y+1, x−1, −z. Lengths of bonds labeled as 1 and 2 (in blue) are given in Table 2. (B) The crystal packing of 1 viewed along c-axis. (C) Stacked layers viewed along b-axis. All hydrogen atoms (B, C) and tetrafluoroborate anions (C) are omitted for clarity.

84x156mm (600 x 600 DPI)

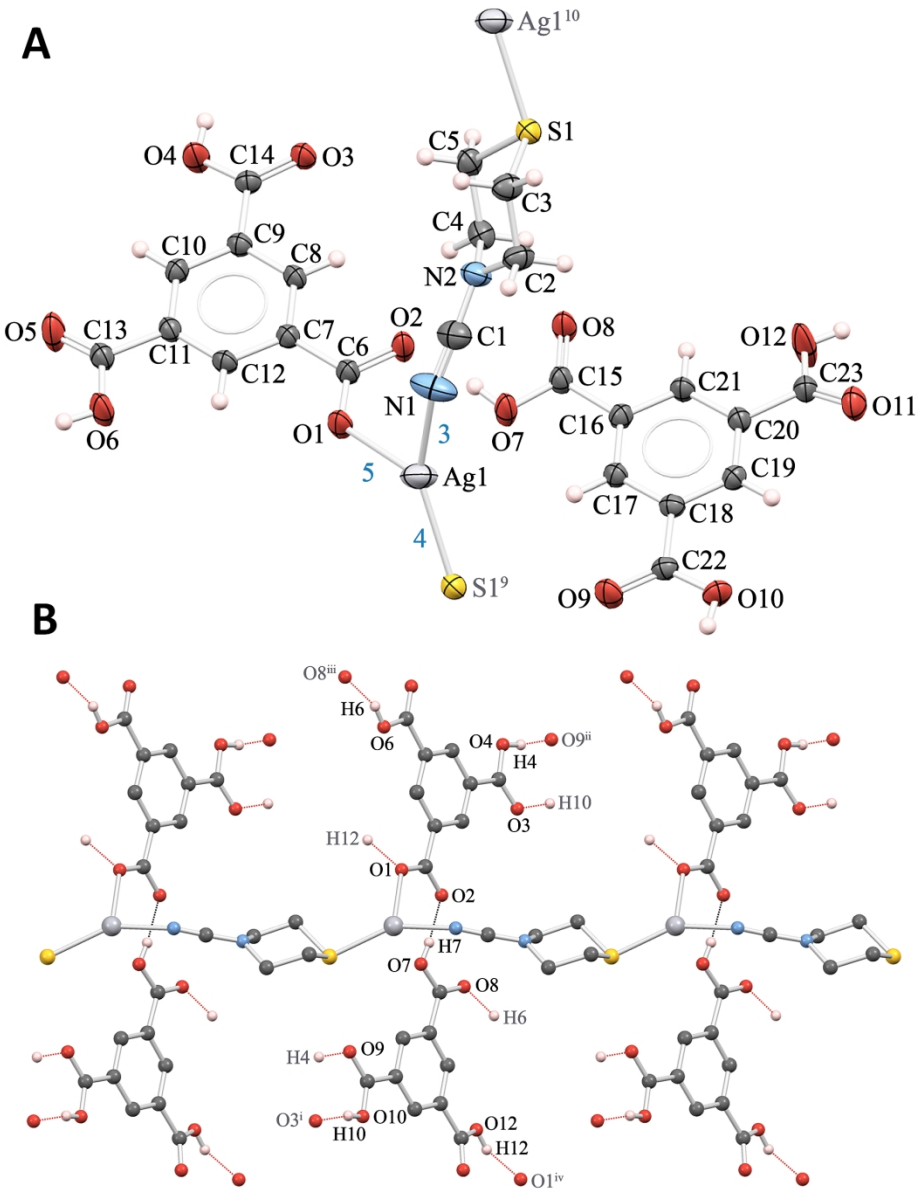

Figure 3. (A) ORTEP drawing (generated by MERCURY93) of the part of infinite structure of 2 with labeled non-H atoms. The atoms of the asymmetric unit are labeled in black. Displacement ellipsoids are shown at the 50% probability level, while the H atoms are drawn as spheres of arbitrary radii. Symmetry codes: (9) x−1, y, z; (10) x+1, y, z. Lengths of bonds labeled as 3–5 (in blue) are given in Table 2. (B) The crystal packing of 2 viewed along c-axis. Selected hydrogen bonds are showed as dashed lines. The hydrogen atoms not involved in the selected hydrogen bonds are omitted for clarity.

84x110mm (600 x 600 DPI)

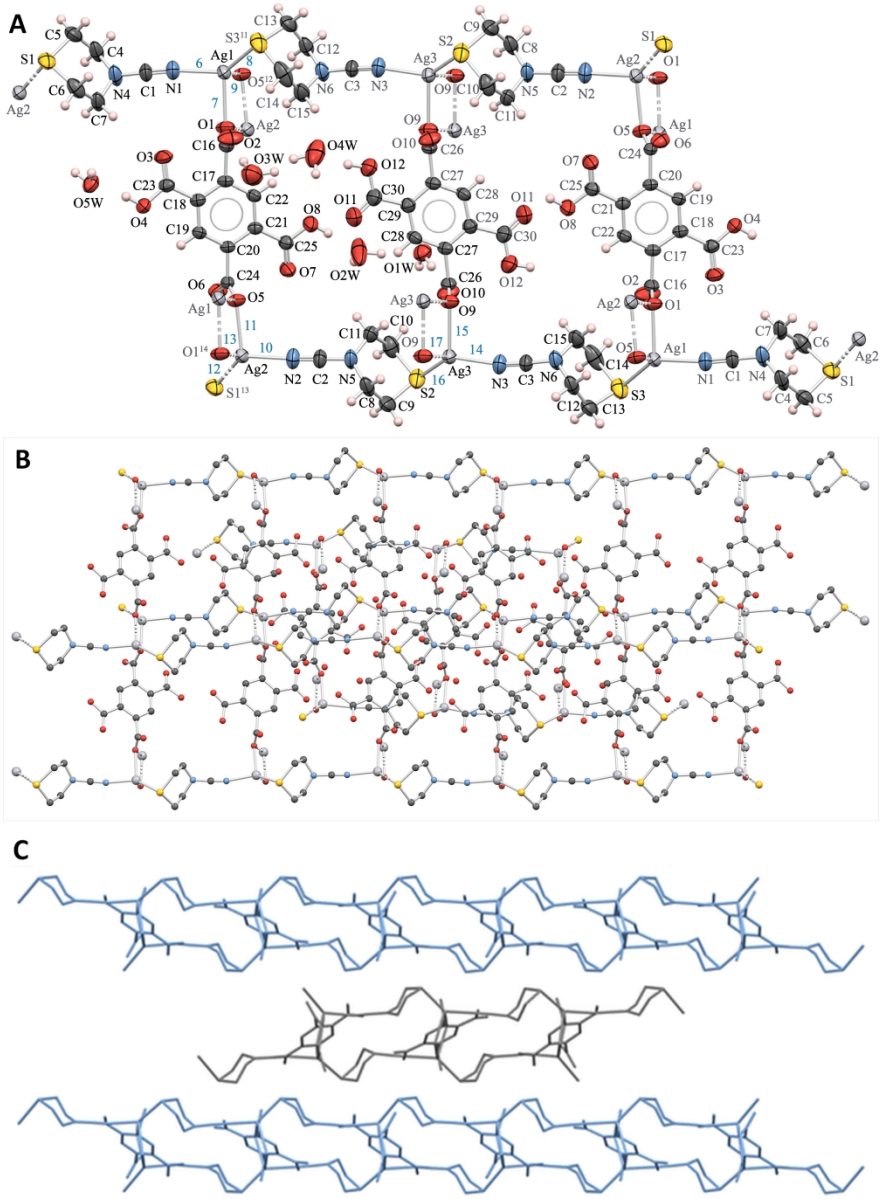

Figure 4. (A) ORTEP drawing (generated by MERCURY93) of the part of infinite structure of 3 with labeled non-H atoms. The atoms of the asymmetric unit cell are labeled in bold. Displacement ellipsoids are shown at the 50% probability level, while the H atoms are drawn as spheres of arbitrary radii. Lengths of bonds labeled as 6–17 (in blue) are given in Table 2. (B) The extended structure of 3 viewed parallel to c-axis. (C) The extended structure of 3 viewed along a-axis showing two-dimensional layers. All hydrogen atoms are omitted for clarity (B, C).

134x184mm (600 x 600 DPI)

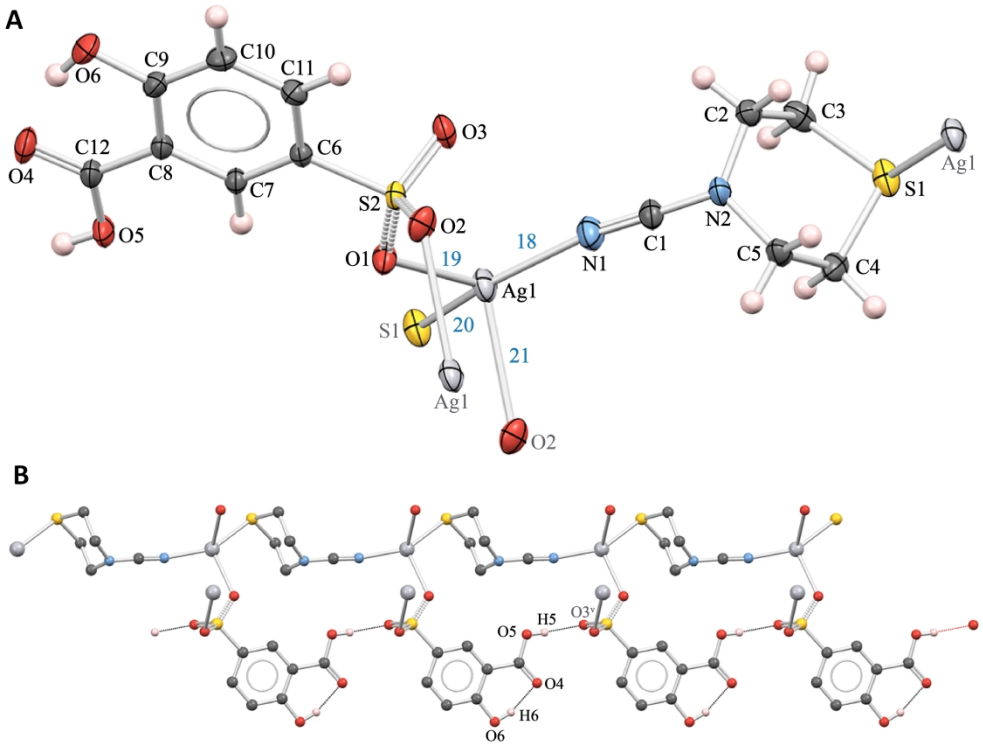

Figure 5. (A) ORTEP drawings (generated by MERCURY93) of the part of infinite structure of 4 with labeled non-H atoms. The atoms of the asymmetric unit cell are labeled in black. Displacement ellipsoids are shown at the 50% probability level, while the H atoms are drawn as spheres of arbitrary radii. Lengths of bonds labeled as 18–21 (in blue) are given in Table 2. (B) The crystal packing of 4 viewed along c-axis. Selected hydrogen bonds are showed as dashed lines. The hydrogen atoms not involved in the selected hydrogen bonds are omitted for clarity.

152x115mm (600 x 600 DPI)

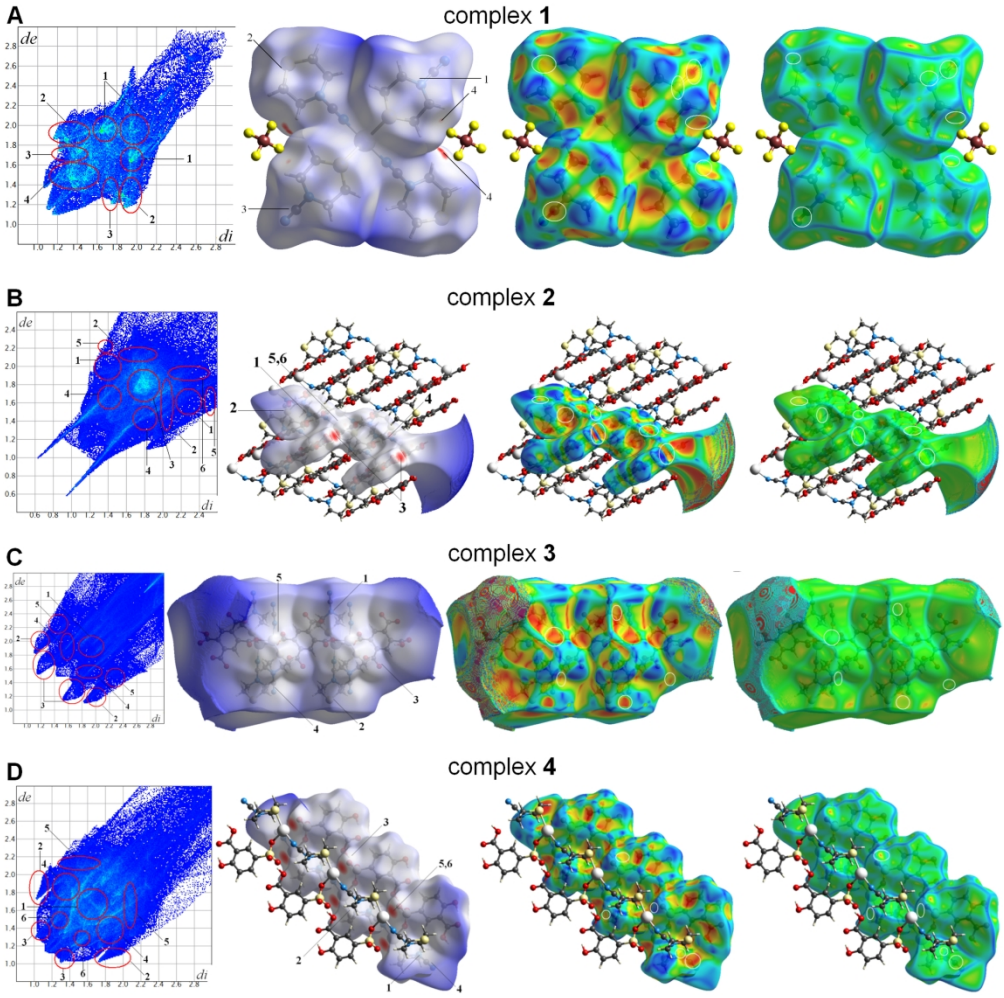

Figure 6. 2D fingerprint plot, Hirshfeld surface mapped with dnorm, shape index and curvedness for 1–4. For interaction types see Table 4.

177x176mm (600 x 600 DPI)

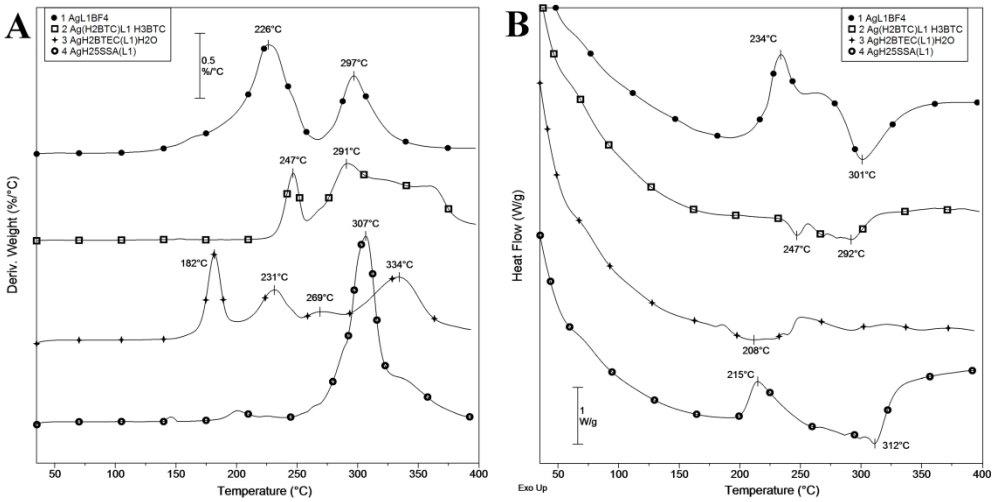

Figure 7. DTG (A) and DSC (B) curves of 1–4 in argon.

182x92mm (600 x 600 DPI)

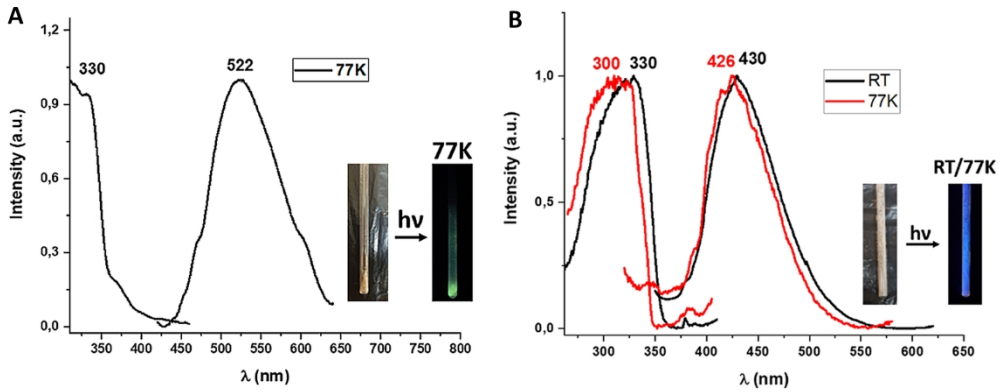

Figure 8. Excitation and emission spectra in solid state at 77K (A) and room temperature and 77 K (B) for 3 and 4, respectively.

174x68mm (600 x 600 DPI)

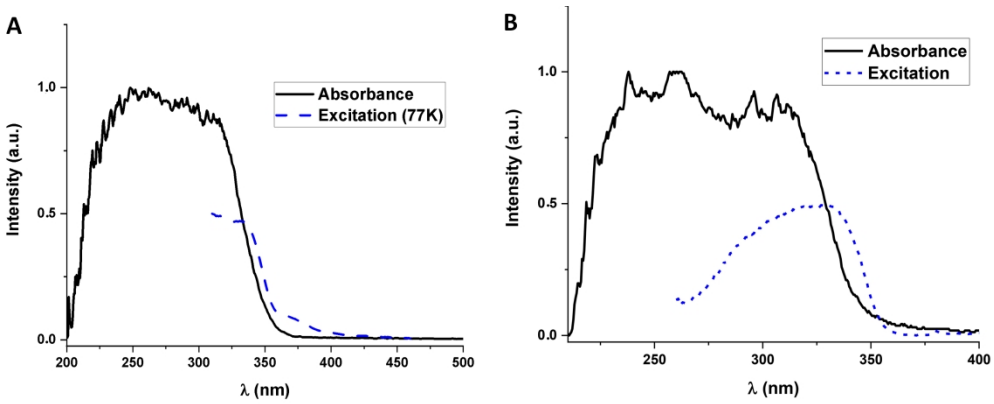

Figure 9. Absorbance (black) and excitation (blue) spectra in the solid state for 3 (A) and 4 (B).

174x69mm (600 x 600 DPI)

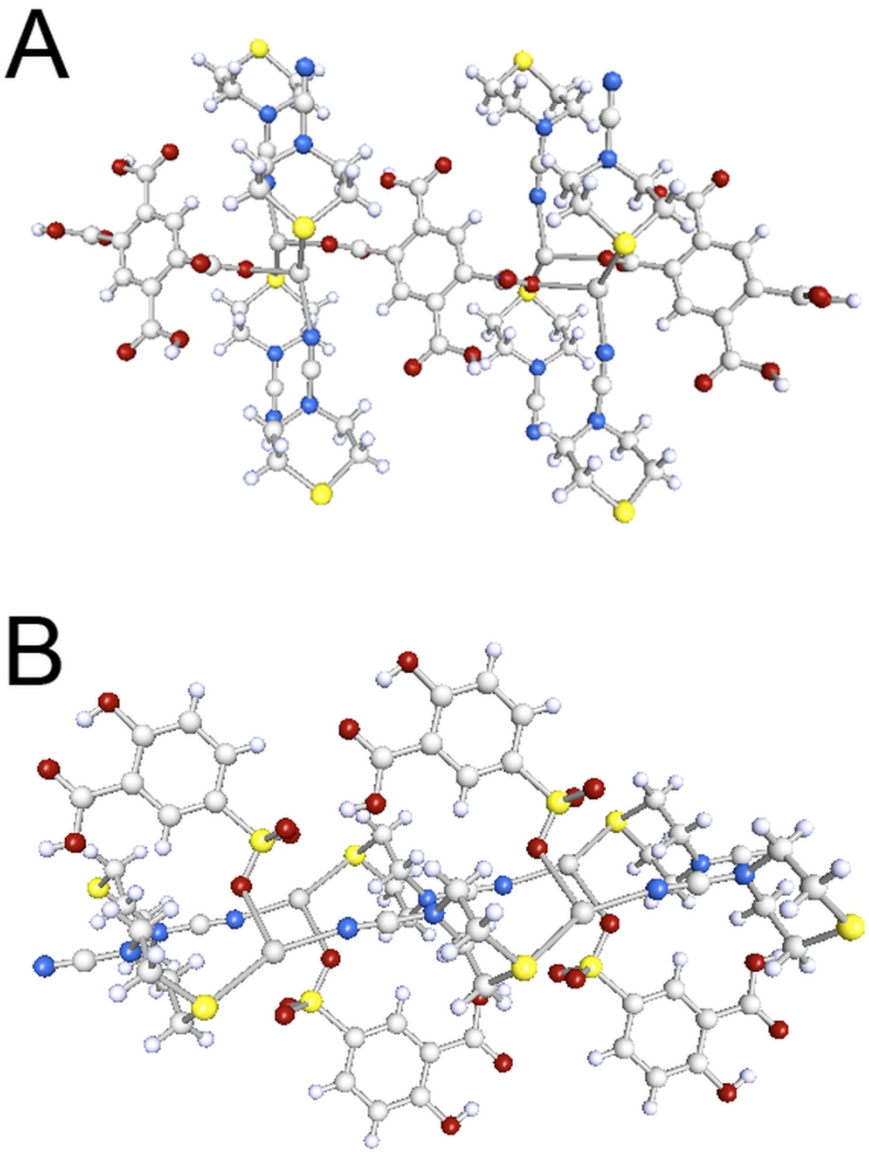

Figure 10. Theoretical model systems representing complex 3 (A) and 4 (B).

84x112mm (600 x 600 DPI)

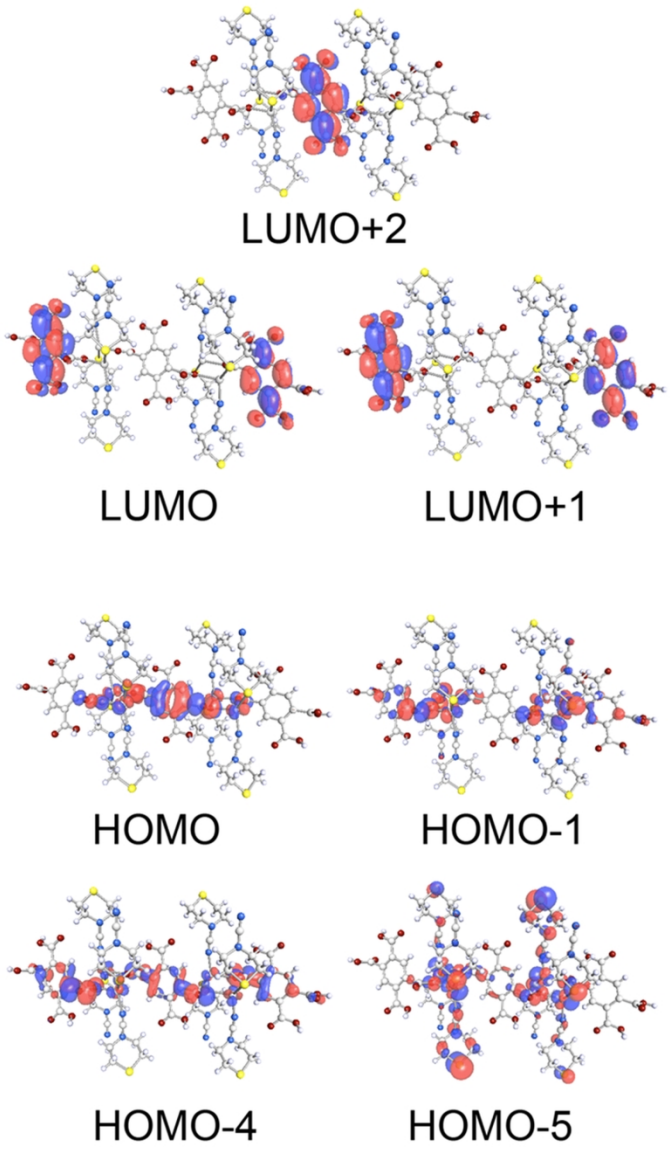

Figure 11. Frontier MOs for model system 3

84x144mm (600 x 600 DPI)

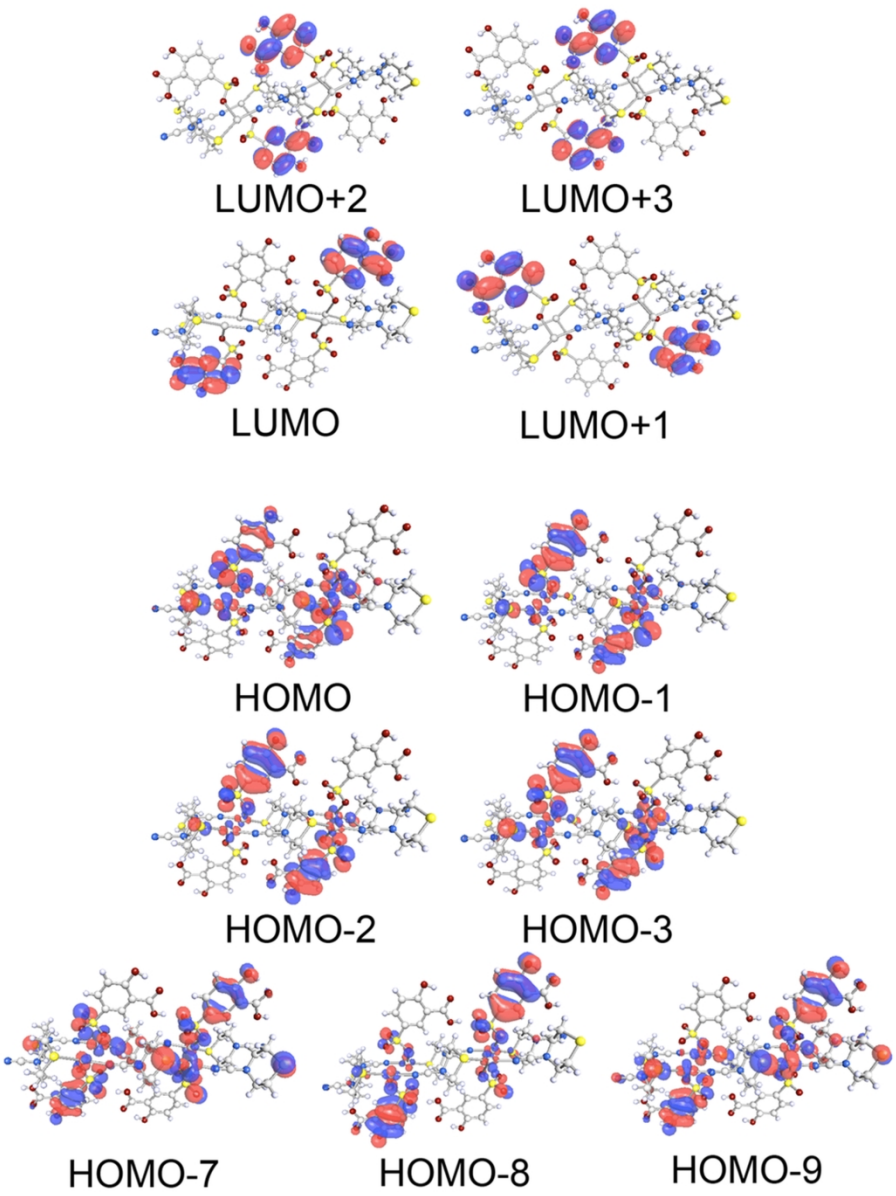

Figure 12. Frontier MOs for model system 4.

84x112mm (600 x 600 DPI)